Advancements in cancer imaging: receptor-targeted approaches for enhanced precision and therapy guidance

Rezaei, S.

Chapter 3

Rectal Cancer Molecular Tumor Imaging using Nanoparticles targeted by a Novel GRPR-binding Peptide for Fluorescence Image-guided Surgery

Somayeh Rezaei, Mark Fonteyne, Luis J. Cruz, Nada Badr, Ajinkya Manelkar, Mahin Saberi, Ronald L.P. van Vlierberghe, Alexander L. Vahrmeijer, Christina Eich, Fernando Albericio, Louise van der Weerd, and Peter J.K. Kuppen.

Materials & Design.
November 2025, 114841. 10.1016/j.matdes.2025.114841

Abstract

Surgical treatment of rectal cancer is difficult due to anatomical complexity. To improve tumor resection, fluorescence-guided surgery (FGS) has been developed using near-infrared fluorescence (NIRF, approximately 800 nm) and a dedicated camera system. Indocyanine green (ICG), an FDA-approved NIRF probe, enables optical imaging. The gastrin-releasing peptide receptor (GRPR), a member of the G protein-coupled receptor family, is widely expressed in rectal cancer cells. This abundant expression makes GRPR an ideal biomarker for molecular targeting and imaging of rectal cancer. In this study, the location and expression levels of GRPR were measured by immunofluorescence, immunohistochemistry and western blot. Our data confirmed significant overexpression of GRPR in rectal cancer cells and tissue samples, providing a significant indication for GRPR targeting evaluation. We designed the novel GRPR-targeting peptide, GRP-derived peptide (GRP-DP) derived from the natural GRPR-binding gastrin-releasing peptide (GRP). The newly developed GRP-DP demonstrated strong in vitro GRPR-targeting capabilities for rectal cancer imaging, potentially aiding surgeons in achieving complete tumor resection. Additionally, we investigated the use of ICG encapsulated within poly(lactic-co-glycolic acid)-polyethylene glycol (ICG/PLGA-PEG) nanoparticles (NPs) as a vehicle for fluorescent tumor imaging in rectal cancer. The ICG-NPs were functionalized with GRP-DP, exhibiting favorable physicochemical properties, including controlled ICG release kinetics and biocompatibility.

1. Introduction

Colorectal cancer (CRC) is a highly prevalent malignancy globally, ranking third in terms of incidence and second in mortality among all cancer types [1, 2]. Rectal cancer constitutes about 30% of colorectal cancers and stands as one of the most prevalent malignancies in high income nations [1, 3, 4]. Surgical resection remains the primary treatment approach for colorectal cancer patients. A significant portion of stage II and III rectal cancer cases may undergo neoadjuvant radiotherapy or chemo-radiotherapy to decrease tumor size and lymph node involvement, reducing the likelihood of local recurrence post-surgery. Given the diverse presentation stages and complexity inherent to rectal cancer, its treatment poses various challenges, spanning preoperative evaluation, surgical intricacies, and postoperative care. Surgery remains the primary curative option for non-metastatic colon and rectal cancers [4-6]. The effectiveness of this surgical method lies in its ability to completely remove cancerous tissue while preserving vital structures and healthy tissue. Near-infrared fluorescence (NIRF) technology, using NIRF-labelled tumor-targeting probes enhances surgical navigation, allowing real-time detection of tumor tissue at various sites, including the primary site, lymph nodes, and other metastatic sites. This approach provides surgeons with visual feedback during cancer surgery, improving safety, thoroughness, and ultimately, oncological outcomes and survival rates [7]. A successful fluorescent probe for medical imaging must meet key requirements, such as optimal wavelength, brightness, stability, specific tissue targeting, and efficient clearance. A common approach is to conjugate a fluorophore to a ligand that binds a cellular receptor, creating an active imaging probe. This allows the probe to accumulate at the target site for enhanced imaging, while non-bound probes must be quickly cleared to reduce background signal [8].

Gastrin-releasing peptide receptor (GRPR), also known as the bombesin receptor 2 (BB2R), belongs to the mammalian bombesin (BBN) receptor family, consisting of three distinct receptors with diverse physiological effects. The human GRPR gene is situated on the X chromosome, encoding a protein with 384 amino acids (AA) and an approximate molecular weight of 43 kDa [9]. The endogenous ligand for GRPR is gastrin-releasing peptide (GRP), which shares a closely related C-terminal peptide sequence with the amphibian peptide bombesin [10]. Both GRP and bombesin exhibit high binding affinity to GRPR at nanomolar concentrations [10]. GRPR expression is identified as a biomarker in prostate and breast cancer, with increased expression observed in various other malignancies, including colon cancer, lung carcinoma, head and neck cancer, renal cancer, and intestinal and bronchial carcinoids [10, 11]. Normal intestinal epithelium lacks endogenous GRPR and other bombesin receptors. However, some CRCs express GRPR and its ligand, GRP, with bombesin activation potentially driving tumor growth in poorly differentiated or aggressive tumors by promoting proliferation, migration, and invasion[12] . Conversely, in well-differentiated tumors, GRP/GRPR expression is linked to better survival, delayed recurrence, and reduced metastasis, possibly due to enhanced differentiation and adhesion to the extracellular matrix, limiting tumor aggressiveness [12]. Due to its common expression in CRC, GRPR is interesting as a target for fluorescent imaging of tumor cells during surgery. BBN7–14, a GRPR agonist, has been widely used to develop GRPR-targeted imaging probes labeled with radionuclides [13] or fluorescent dyes [14]. Over the past two decades, extensive efforts in developing radiolabeled and fluorescently labeled BBN analogues have yielded promising results in both preclinical and clinical studies [15]. High-affinity NIRF-labeled GRPR probes also hold great potential for image-guided and intraoperative surgery [16].

Indocyanine green (ICG) is a water-soluble, anionic fluorescent molecule with a molecular weight of 751 Da. It exhibits absorption and fluorescence emission in the near-infrared (NIR) wavelength region [17, 18]. The application of ICG in colorectal cancer surgery is gradually increasing due to its ability to enhance intraoperative tumor imaging for improved diagnostic accuracy [19]. ICG is a cost-effective and straightforward compound widely employed in abdominal surgery, and is particularly beneficial in colorectal and rectal surgery. It enables real-time intraoperative assessment of the blood supply to the remaining portions of the large intestine following resection and to the intestine after anastomosis, thereby reducing the risk of anastomotic leaks [20-23]. Nevertheless, despite its numerous benefits, the clinical use of ICG is accompanied by certain limitations. Following intravenous administration, ICG readily binds non-specifically to plasma proteins and undergoes rapid clearance (with a plasmatic half-life of approximately 2-4 minutes), primarily due to reticuloendothelial system (RES) activity [24, 25]. In addition to inherent physicochemical property issues, ICG lacks tumor targeting specificity, limiting its use for precise cancer imaging [17]. Several strategies have been investigated to improve the specificity and targeting of ICG for rectal cancer [22]. Recent research suggests that incorporating ICG into nanoparticles (NPs) holds promise for overcoming existing limitations and serving as an ideal targeting vehicle for image-guided applications. This approach enhances the stability of ICG, prolongs its circulation time, and facilitates its accumulation in tumors. ICG can be loaded, doped, or conjugated to various types of NPs, which can then be further functionalized with ligands to enable specific tumor targeting [26, 27].

Poly(lactic-co-glycolic acid-polyethylene glycol) (PLGA), an FDA-approved copolymer, is extensively used for creating NPs in biomedical drug delivery systems due to its biodegradability, biosafety, biocompatibility, and versatility [28]. PLGA-based nanocarriers improve the bioavailability of drugs by protecting them from premature degradation. They allow for sustained and targeted drug delivery, adjustable degradation kinetics, enhanced intracellular penetration, and reduced side effects [28-30]. Recent studies have provided a comprehensive examination of covalent and non-covalent approaches used to functionalize biodegradable NPs with tumor-targeting peptides [31]. Peptide ligands offer advantages to other targeting agents due to their small size, affordability, specificity, and flexibility in sequence and conjugation. When linked to imaging agents or nanocarriers, they enhance on-site delivery, improving tumor imaging and chemotherapy effectiveness while minimizing side effects. Consequently, certain peptides, either alone or in combination with other agents, have entered clinical trials, demonstrating good tolerance and low toxicity [32]. Targeting exploits the overexpression of specific receptors on cancer tissue compared to healthy cells [33]. In this study, we investigated the expression of GRPR in rectal cancer, designed a novel GRPR-targeting peptide, and developed GRPR-targeted ICG-NPs for molecular tumor imaging. The novel GRPR-targeting peptide conjugated with ICG-NPs was employed to enhance fluorescence image-guided surgery, aiming to improve the precision of rectal cancer detection and treatment.

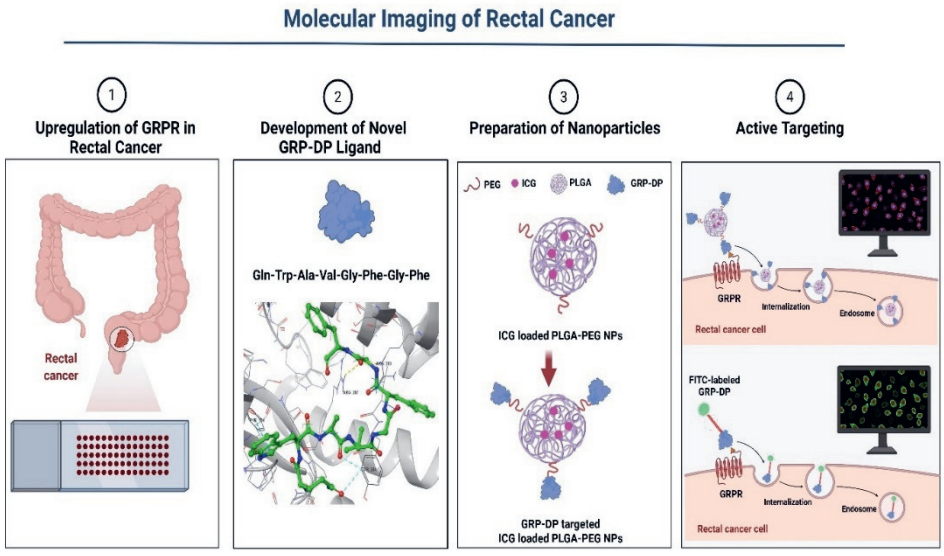

Scheme 1. Schematic representation of molecular imaging of rectal cancer using GRP-DP-targeted ICG/PLGA-PEG nanoparticles. The nanoparticles, functionalized with gastrin-releasing peptide receptor (GRPR) ligands, enable targeted imaging of rectal cancer cells. Indocyanine green (ICG) serves as the fluorescent probe, while the PLGA-PEG nanoparticle system enhances stability, biocompatibility, and tumor accumulation. This targeted imaging approach improves cancer detection and provides a potential strategy for image-guided diagnosis.

2. Materials and Methods

2.1. Chemicals used

PLGA (PURASORB® PDLG 5002A 50:50, with an inherent viscosity of 0.20 dL/g, MW = 17,000) was obtained from Carbion PURAC (Amsterdam, the Netherlands). The solvents used for synthesizing PLGA NPs, including dichloromethane (DCM; CAS 75-09-2) and polyvinyl alcohol (PVA; CAS 9002-89-5), were sourced from Sigma-Aldrich (Zwijndrecht, the Netherlands). Chloroform was obtained from Merck (Darmstadt, Germany). Lipid-PEG 2000 (1,2-distearoyl-sn-glycero-3-phosphoethanolamine-N-[methoxy(polyethylene glycol)-2000]) and DSPE-PEG2000-NHS (1,2-distearoyl-sn-glycero-3-phosphoethanolamine-N-[methoxy(polyethylene glycol)-2000-N-hydroxysuccinimide]) were obtained from Nanocs Inc. (New York , USA). The PLGA-PEG NPs were all loaded with ICG purchased from Lumiprobe (Hannover, Germany). PEG denotes a polydisperse polyethylenglycol with a molecular weight average of 2000.

2.2. Antibodies

Anti-GRPR Rabbit Polyclonal antibody (USBI036320) and Goat Anti-Rabbit IgG H&L (Alexa Fluor® 488) were purchased from Avantor (Hillegom, the Netherlands) and Abcam (Cambridge, United Kingdom) respectively . Anti- GRPR antibody (#ABR-002) was purchased from Alomone Labs (Jerusalem, Israel) . Anti-beta Actin antibody-Loading control (ab 8229) and IRDye 800CW Goat anti-Rabbit IgG Secondary Antibody (NC9401842) were obtained from Abcam and LI-COR (Lincoln, Nebraska, USA) respectively . 4’,6-diamidino-2-phenylindole (DAPI) and To-pro 3 iodide (642/661) were purchased from Invitrogen (Thermo Fisher Scientific, Waltham, MA, USA). The human GRPR protein (#RPU52625) was obtained from Biomatik (Ontario, Canada).

2.3. Cell culture

Fetal bovine serum (FBS), Modified Eagle’s Medium (DMEM), Roswell Park Memorial Institute (RPMI) medium, trypsin, and penicillin-streptomycin (10,000 U/mL) were obtained from Gibco Laboratories (Thermo Scientific™, Waltham, Massachusetts, USA). [3-(4,5-dimethylthiazol-2-yl)- 5-(3-carboxymethoxyphenyl)-2-(4-sulfophenyl)-2H-tetrazolium (MTS) was supplied by Promega (Leiden, the Netherlands). The SW837 (ATCC-CCL-235) and SW1463 (ATCC-CCL-234) rectal adenocarcinoma cell lines, along with the Jurkat (acute T cell leukemia) cell line, were cultured in RPMI, while HT29 (ATCC HTB-38) colon adenocarcinoma, PC-3 (ATCC CRL-1435) prostate adenocarcinoma, and HEK-293T (ATCC CRL-11268) human embryonic kidney cell lines were cultured in DMEM. All media were supplemented with 1% penicillin-streptomycin and 10% FBS, and cells were maintained at 37°C with 95% relative humidity and 5% CO_2.

2.4. Targeting peptides

Targeting peptides, including gonadotropin releasing hormone (GnRH); pGlu-His-Trp-Ser-Tyr-DLeu-Leu-Arg-Pro-PEG-NH2 [34, 35] (where PEG is monodisperse amino-PEG3-acyl), novel GRP-DP; Ac-Gln-Trp-Ala-Val-Gly-Phe-Gly-Phe-Lys-PEG-NH2 were synthesized by the solid-phase peptide synthesis method, purified by high-performance liquid chromatography (HPLC) and characterized by electrospray mass spectrometry. FITC-labeled GRP-DP and GRP Scrambled peptide (GRP-SP) (Ac-Trp-

Val-Gly-Ala-Gln-Phe-Lys-PEG-Phe-Gly-NH2) were provided by GL Biochem Ltd. (Minhang, Shanghai, China).

2.5. Western blot assay (WB)

The previously mentioned cell lines were collected for the WB experiment. The cells were lysed using Radioimmunoprecipitation Assay (RIPA) buffer and scraped to obtain the protein supernatant after centrifugation at 15,000 × g for 15 minutes (min) at 4°C. Total protein samples were heated for 5 min at 95˚C with Laemmli buffer containing 10% v/v β-mercaptoethanol (Sigma-Aldrich, MO, USA, catalog # M3148) and loaded on 10% SDS-PAGE gels and subjected to electrophoresis. Subsequently, they were transferred to a polyvinylidene fluoride (PVDF) membrane using a transfer system at 150 V for 1 hour (h). To block nonspecific binding, the membrane was incubated with a blocking solution consisting of 5% skim-dried milk powder in PBST 1% (Phosphate-Buffered Saline (PBS) containing 0.1% Tween 20) for 1 h at room temperature (RT). The primary antibodies, including anti-GRPR antibody Avantor (Hillegom, the Netherlands) were diluted in blocking buffer with PBST at a dilution of 1:100. Additionally, a rabbit monoclonal antibody against β-actin was diluted in 10 mL at a dilution of 1:2000. The membrane was then incubated with these primary antibodies overnight at 4°C. Following the primary antibody incubation, the membrane was washed three times with 1% PBST to remove unbound antibodies. Subsequently, it was incubated with a Rabbit IRDyeR680CW-labeled secondary antibody, diluted at 1:5000 in blocking buffer with PBST for 30 min at RT. After a final wash three times with PBST, the membrane was imaged using an Odyssey Infrared Imager 9120 (LI-COR) scanner (The Lab World Group, Hudson, MA, USA) at an excitation wavelength of 700 nm to detect the binding of the antibodies. The obtained results were analyzed using ImageJ software (version 1.53a) or a similar tool.

2.6. Immunofluorescence (IF) analysis of GRPR receptor expression in rectal cancer cells

2.6.1. Cytospin method for processing cell suspensions

SW837, SW1463, PC-3, HT29, HEK-293T and Jurkat cells were cultured and subjected to trypsinization. The resulting cell suspension, containing 10-25 $\times 10^3$ cells in 50 µl of PBS, was loaded into a Thermo Shandon Cytospin 3 Centrifuge (Massachusetts, USA) according to the manufacturer's protocol [36]. The cells were centrifuged at 500 revolutions per min (rpm) for 5 min. The slides were then air-dried at RT and stored at -20˚C for future use.

2.6.2. Immunofluorescence (IF) staining of cytospin preparations: processing of slides

To investigate the cellular localization of GRPR, cytospin-prepared slides cells were first fixed with 4% paraformaldehyde (PFA). Cells were then permeabilized in 0.2% (v/v) TritonX-100 in PBS for 10 min at RT and blocked with 5% PBSA at RT for 30 min. The primary antibody, anti-GRPR antibody Avantor (Hillegom, the Netherlands) was applied to the cells (dilution 1:100) overnight at 4˚C, followed by incubation with Goat Anti-Rabbit IgG H&L (Alexa Fluor® 488) secondary antibody (dilution 1:1000). After washing and staining the cell nuclei with Hoechst 33342 (1:1000) for 15 min, the slides were imaged using a CLSM Leica TCS SP8 (Leica Microsystems, Wetzlar, Germany) [37-39].

2.7. Patient material

The study cohort included patients from the non-preoperative treated arm of the Dutch TME trial (1996-1999, DUT-KWF-CKVO-9504, EORTC-40971, EU-96020), which evaluated TME surgery with or without preoperative radiotherapy (5 × 5 Gray) [40]. Radiotherapeutic, surgical, and pathological procedures were standardized and quality-controlled. The Leiden University Medical Center's Medical Ethical Committee approved the trial and retrospective use of samples, with all patients providing written informed consent. A tissue microarray (TMA) was previously constructed [41]. The study included 216 rectal cancer patients with sufficient formalin-fixed paraffin-embedded tumor material who underwent surgery without preoperative radiotherapy.

2.7.1. Immunohistochemical staining of GRPR

To evaluate GRPR expression, we conducted an immunohistochemical analysis following a precise protocol to ensure accurate and reproducible results. Tissue sections of 4-6 µm thickness were prepared on slides and dried overnight at 37°C. Deparaffinization involved three 5-min incubations in Xylol. The slides were then rinsed three times in absolute ethanol and rehydrated through 70% and 50% ethanol. To block endogenous peroxidase activity, the slides were incubated for 20 min in a 0.3% PBS/H_2O_2 (Merck) solution. Antigen retrieval was performed using Envision Flex Target Retrieval Solution pH 6 (Dako) with a DAKO PT-link system. Slides were warmed up to 95°C and kept at that temperature for 10 min. After cooling, the slides were washed twice in PBS, then incubated overnight with the GRPR primary antibody (Alomone Labs; Clonename) at predetermined optimal dilution in PBS containing 1% BSA. The following day, the slides were washed three times in PBS to remove unbound primary antibody and incubated for 30 min with an undiluted Envision anti-rabbit-HRP-polymer (Dako) secondary antibody. After three more PBS washes, the slides were developed using a DAB-kit (Dako), producing a brown precipitate indicating the presence of the target antigen. Finally, slides were counterstained using Haematoxilin to visualize the nuclei of the cells.

2.7.2. Scoring method

The intensity of GRPR expression, as determined by immunohistochemical staining, in tumor tissues was assessed as follows: negative (all tumor epithelium negative), mixed (both positive and negative tumor epithelium cells in a tumor), and positive (all tumor epithelium positive). Rectal cancer tissues were analyzed in a double-blinded manner to ensure unbiased assessment.

2.8. Docking study of GRP-derived peptide

Peptide–protein docking of the GRP-derived peptide (GRP-DP; Gln-Trp-Ala-Val-Gly-Phe-Gly-Phe) was conducted using AutoDock-CrankPep (ADCP) v1.0 rc1, a dedicated software developed by The Scripps Research Institute for predicting peptide binding conformations. ADCP scores it's predictions based on a pose scoring method using a *CRANKITE*'s *Gō*-Type potential and Ramachandran propensities for backbone ϕ and ψ angles, which are transformed into energies according to the Boltzman distribution [42]. This internal score is then combined with an interaction score between the peptide and the protein that is calculated using *AutoDock* affinity grids, resulting in a ADCP-score. A cryogenic electron microscopy (cryo-EM) derived structure of GRPR with a resolution of 3.0 Å was obtained from the RCSB Protein Data Bank (PDB-id: 7W3Z) [43]. The GRP peptide that was co-crystalized in complex with the GRPR receptor was removed from the binding pocket and the C-terminal sequence of GRP/BBN

(Trp-Ala-Val-Gly-His-Leu-Met) was docked to the binding site using ADCP as a positive control. The conformation of the GRP/BBN sequence and the GRP-DP sequence were generated with MODDELER (Version 10.5). Before docking, the GRP-DP, GRP/BBN and the receptor GRPR were protonated and NQH-groups were rotated and flipped using 'Reduce' software software version 4.9 [44] Existing rotatable groups, lysine NH3, and existing OH & SH groups were allowed to rotate. GRP-DP and the GRP/BBN were docked using 200 independent ADCP runs (N=200). Given that the longest peptide, GRP, consists of 12 amino acids (AA), and based on the ADCP documentation, which recommends performing 1 million Monte Carlo (MC) evaluation steps per amino acid, we opted to conduct a total of 12 million evaluations (n = 12000000) for the scoring function. The docking run was performed twice with the seeds 42 and 1997. The mean, median, and top affinity values were derived from the top 10 results of each ADCP run. We opted to focus on the top 10 results because including all results, particularly those with low affinity, skewed the distribution, significantly reducing the sensitivity of the analysis. This approach ensured that high-affinity interactions, which are most relevant for differentiating between peptides, were emphasized without the dilution caused by lower-affinity outcomes. Schrodingers Meastro software (version 14.2, Schrodinger, LLC, New York, USA) was used for the visualization of peptide interactions in complex with GRPR.

2.8.1. Fluorescence polarization binding assay

In the fluorescence polarization (FP) saturation binding experiments, 100 nmol/L of FITC-labeled GRP-DP was incubated in triplicate with increasing concentrations of human GRPR protein (#RPU52625, Biomatik, Ontario, Canada) in H_2O, ranging from 0.478 µmol/L to 15.32 µmol/L. The FP signals were recorded 10 min after incubation at RT. All FP measurements were conducted using a multifunctional microplate reader (EnVision, PerkinElmer, Waltham, United States) in black 384-well microplates (Corning, Cat No 3575), with 10 µL of peptide solution and 10 µL of human GRPR solution per well. For FP measurements, a BMG LABTECH machine (Ortenberg, Germany) was used with 480 nm excitation and 535 nm emission filters. Data were analyzed using MARS data analysis software (version 3.20 R2) [45].

2.9. Preparation of ICG/PLGA-PEG NPs

The ICG/PLGA-PEG NPs (ICG-NPs) were synthesized using an oil/water emulsion and solvent evaporation-extraction method. Initially, 100 mg of PLGA was dissolved in 3 mL of DCM containing 2 mg of ICG. This solution was then added to 25 mL of 2.5% (w/v) polyvinyl alcohol (PVA) aqueous solution and emulsified for 2 min using a sonicator (250 watt; Sonifier 250; Branson, Danbury, USA). Subsequently, the emulsified solution was transferred to a new vial of 300 µL chloroform containing 12 mg of DSPE-PEG2000-NHS and 10 mg of DSPE-PEG2000, followed by air drying. The mixture was homogenized for 1 min using sonication. After 3 h of solvent evaporation at 4°C, the ICG-NPs were collected by centrifugation at 21000 g for 30 min at 4°C. The NPs were then washed three times with distilled water and lyophilized for 3-4 days [46, 47].

2.10. Conjugation of the targeting peptides to ICG-NPs

To conjugate the targeting peptides to the prepared ICG-NPs, 10 mg of ICG-NPs were dissolved in 500 µL of bicarbonate buffer (pH 8-9) and mixed with 500 µg of targeting peptides (GnHR and GRP-DP) in PBS. The mixture was incubated at RT for 1 h, followed by overnight incubation at 4°C. The targeted

GnHR and GRP-DP ICG-NPs (GnHR@ ICG-NPs and MP-GRP@ ICG-NPs) were obtained by centrifuging the mixture at 21000 g for 30 min. The supernatant was collected to determine the amount of unconjugated peptide using Coomassie blue [48].

2.11. Characterization of NPs

2.11.1. Morphology and size characterization

The morphology of the NPs was examined using transmission electron microscopy (TEM). Carbon-coated grids (Formvar/Carbon on 200 Mesh Copper; AGS162; Van Loenen Instruments; Zaandam, the Netherlands) were glow-discharged using the Emitech K950X Turbo Evaporator (Quorum Technologies; Ashford, UK) at $2x10^{-1}$ bar and 20 mA for 1 min before staining. A 3 µL sample solution was applied to the glow-discharged grid and allowed to adhere for 1 min. Excess liquid was removed by blotting onto a filter paper, and then 3 µL of 2% uranyl acetate in distilled water was added to the grid for negative staining. After 1 min, excess uranyl acetate was removed by blotting, and the sample was air-dried for 10 min. The grids were mounted on a RT holder and examined using a Tecnai 12 Twin microscope (FEI Company; Hillsboro, Oregon, USA) equipped with a OneView Camera Model 1095 (Gatan; Pleasanton, California, USA) at a voltage of 120 kV. Digital images were acquired and stored using Digital Micrograph 3.4 software (Gatan). The average size and zeta potential of the NPs were determined using Dynamic Light Scattering (DLS) (Zetasizer Nano S90, Malvern Instruments, Worcestershire, Cambridge, UK). Briefly, the NPs were dispersed in water and analyzed at 25°C. Zeta potential (Zetasizer Nano S90) was used to assess the stability and aggregation of the NPs. Each sample was measured in triplicate, and the averages and standard deviations were calculated [46, 49].

2.11.2. Encapsulation efficiency analysis of ICG

To calculate the encapsulation efficiency (EE) and the loading content (LC) of ICG, the ICG-NPs were dissolved in 0.8 M NaOH overnight, then the solution was centrifuged at 12,000 rpm and the supernatant was collected [50]. The ICG amount was measured by the Odyssey Infrared Imager 9120 (LI-COR) scanner at 800 nm. The EE and LC for ICG were calculated thus [51, 52] :

$$EE\ (\%) = \frac{(\text{Amount of all of the encapsulated ICG in the ICG-NPs}}{\text{Amount of all of the added ICG}} \times 100 \quad (1)$$

$$LC\ (\%) = \frac{(\text{Amount of all of the encapsulated ICG in the ICG-NPs}}{\text{Amount of the ICG-NPs}} \times 100 \quad (2)$$

2.11.3. Optical properties of ICG

After the preparation of ICG-NPs, 50 µL of ICG-NPs (20 mg/mL) and free ICG (1 mg/mL) were diluted with water. Absorbance and fluorescence were then measured using a SpectraMax® iD3 multi-mode microplate reader (Molecular Devices, USA).

2.11.4. Study of ICG release from NPs

The release of ICG from ICG-NPs, GnRH@ICG-NPs and GRP-DP@ICG-NPs was studied [53]. Lyophilized NPs (2 mg) were dissolved in 2 mL of PBS at pH 7.4 and stirred at 37°C. At specific time intervals: 1, 2, 3, 4, 6, 12, 24, 48, 72, 120, 144, and 192 h. the NPs solution was centrifuged at 12,000 rpm for 20 min, and 150 µL of the supernatant was collected. Subsequently, 150 µL of fresh PBS was added to the

remaining NPs. The released ICG in each sample was detected using an Odyssey Infrared Imager 9120 (LI-COR) at 800 nm.

2.12. Cell preparation for live-cell imaging with FITC-labeled peptide

Fluorescence microscopy was used to evaluate the localization and uptake of FITC@GRP-DP and FITC@GRP-SP in various cell lines. FITC@GRP-DP uptake was analyzed in all specified cell lines (excluding Jurkat), while FITC@GRP-SP was tested specifically in PC3 cells. Cells were cultured, trypsinized, and washed with PBS. Subsequently, 40,000 cells per well were transferred into 400 µL of medium in chamber slides (µ-Slide 8 Well Glass Bottom, ibidi GmbH, Germany) and incubated at 37°C for 24 h. After the incubation period, the medium was carefully removed, and the cells were washed twice with 1% PBS/BSA (150 µL per well). Next, the cells were stained for 15 min with Hoechst 3342 at a dilution of 1:1000 in PBS/BSA (1%) followed by a wash with PBS/BSA (1%) .The cells were then treated with 2.5 , 10 and 20 µM of FITC@GRP-DP in FBS-free medium (100 µL/well) at 37°C for 60 min and washed once with PBS/BSA (1%). Finally, the cells were resuspended in 300 µL of PBS and followed for imaging of live cell imaging microscopy Dragonfly 200 spinning disk (Andor Technology, Belfast, United Kingdom) [54].

2.13. Cell viability assay

Cell viability was assessed using the MTS assay. Briefly, 10,000 SW737 and SW1463 cells per well were seeded and overnight cultured in 96-well plates. The following day, the cells were treated with various formulations including ICG-NPs, GnRH@ICG-NPs, and GRP-DP@ICG-NPs at concentrations of 80, 100, 200, and 500 µg/mL for 24, 48, and 72 h. After each incubation period, RPMI medium (100 µL per well) was mixed with MTS solution (20 µL per well), followed by a 2 h incubation. The absorbance was measured at 490 nm using a SpectraMax M3 Multi-Mode Microplate Reader (Molecular Devices, Silicon Valley, CA, USA)[55] .

2.13.1. Study of the uptake of NPs by optical imaging

For the uptake study, SW837 and SW1463 cells (10×10^3 cells per well) were seeded in a 96-well Black Microplate (Greiner Bio-One CELLSTAR µClear™ 96-well, Cell Culture-Treated, Flat-Bottom Microplate) and incubated at 37°C for 24 h. The following day, the cells were treated with various formulations including ICG-NPs, GnRH@ICG-NPs, and GRP@ICG-NPs for 1, 2, 4, and 8 h. Subsequently, the cells were washed with PBS and fixed with 2% paraformaldehyde (PFA). The cell nuclei were stained with TO-PRO®-3 iodide (1:1000 dilution; Molecular Probes, Thermo Fisher, Marietta, OH, USA) for detection at 700 nm. [56]. Following TO-PRO®-3 staining, which allows for the detection of the cell nucleus at 700 nm, the wells were washed with PBS, and the plates were scanned using an Odyssey Infrared Imager 9120 (LI-COR) at wavelengths of 800 nm and 700 nm to measure the content of ICG and TO-PRO®-3 respectively.

2.13.2. Study of the uptake of NPs by fluorescence microscopy

SW837 cells were seeded into circular cover glasses (Oxford Instruments, United Kingdom) in a 24-well plate at a density of 10×10^4 cells per well (300 µl). After 24 h, the culture medium was replaced with ICG-NPs, GnRH@ICG-NPs, and GRP-DP@ICG-NPs in serum-free medium at a concentration of 40 µg/mL of NPs. The cells were incubated for 1, 2, 4, and 8 h, then washed with PBS and fixed with a 4%

PFA solution for 15 min. The cell nuclei were stained with DAPI for 10 min. Finally, the cover glasses were washed with PBS, mounted using Aqua Poly/Mount (Polysciences), and observed using fluorescent microscopy (Leica DMRA fluorescence microscopy, LUMC, University of Leiden [57].

3. Statistical Analysis

GraphPad Prism 8.1.1 software (GraphPad Software, San Diego, CA, USA) was used for statistical analysis. Unless otherwise stated, all data are expressed as the mean ± standard deviation (SD) of 3-5 independent repeated experiments. The data were statistically significant by Student's *t*-test, unpaired, Mann-Whitney U test, and two-way analysis of variance (ANOVA). In all analyses, a *p*-value ≤ 0.05 was considered an indicator of statistical significance and is expressed as: # (not significant, $p \geq 0.05$) * $p \leq 0.05$, ** $p \leq 0.01$, *** $p \leq 0.001$, **** $p \leq 0.0001$. For analyzing the clinical data, statistical analyses were conducted using SPSS version 17.0 for Windows (SPSS Inc.).

5. Results

GRPR is upregulated in Rectal Cancer

GRPR is highly expressed in CRC cells, making it a key biomarker in CRC progression and a promising target for molecular imaging, diagnostics, and targeted therapies [58, 59]. This study assessed its expression and localization in rectal cancer cell lines for potential use in fluorescence-guided surgery and other clinical applications. To achieve this, we systematically analyzed GRPR expression and distribution across cell lines using multiple techniques, guided by data from the Human Protein Atlas [60]. The initial analysis revealed varying GRPR expression, with PC3 and HT29 showing higher levels, while HEK-293T and Jurkat exhibited little to no expression. Rectal cancer cell lines including SW837 and SW1463 were included for further analysis. Western blot analysis was performed to validate and quantify GRPR expression levels from the initial screening. This approach confirmed the presence of GRPR protein and allowed measurement of its relative expression using ImageJ software. The results demonstrated GRPR expression in PC3, HT29, SW837, and SW1463 cancer cells, while HEK-293T and Jurkat cells showed no detectable expression (Figure 1A). Western blot analysis further validated GRPR expression in rectal cancer cells, offering critical insights into its role in this study. We next examined the cellular distribution of GRPR in Cytospin-prepared, fixed cells using confocal microscopy. Immunofluorescence staining with an anti-GRPR antibody revealed detectable GRPR signals at both the cell membrane and within the cytoplasm of GRPR-positive cells. Confocal imaging further confirmed strong GRPR expression in PC3, HT29, SW837, and SW1463 cells (Figure 1B). In contrast, GRPR-negative control cells, including HEK-293T and Jurkat cells, exhibited no detectable staining [61]. GRPR expression in rectal tumors was analyzed using IHC on tissue samples from 216 patients, revealing its predominant localization in the tumor epithelium, particularly at the cell membrane and within the cytoplasm. The intensity and distribution of GRPR expression varied among samples, with some tumors exhibiting strong, uniform staining, while others displayed heterogeneous or mixed expression patterns (Figure 2A, B). None of the patients exhibited a complete absence of GRPR expression in the tumor epithelium. Strong brown cytoplasmic staining for GRPR in rectal cancer cells was observed, while stromal cells showed weak background or absent staining in most samples. This weak stromal staining may be attributed to the role of GRPR in immune cell regulation, with aberrant expression linked to the pathogenesis of inflammatory conditions [62]. Due to staining artifacts and material loss during the IHC procedure, 89 out of 216 tumor samples could not be

analyzed. Among the evaluable samples, 14 (11%) exhibited mixed GRPR expression (partial positivity), while 113 (89%) demonstrated full GRPR positivity (Figure 2C). These results, obtained through multiple analytical techniques, provide strong evidence that GRPR is consistently expressed in rectal cancer cells, supporting its potential as a biomarker for diagnostic and therapeutic applications.

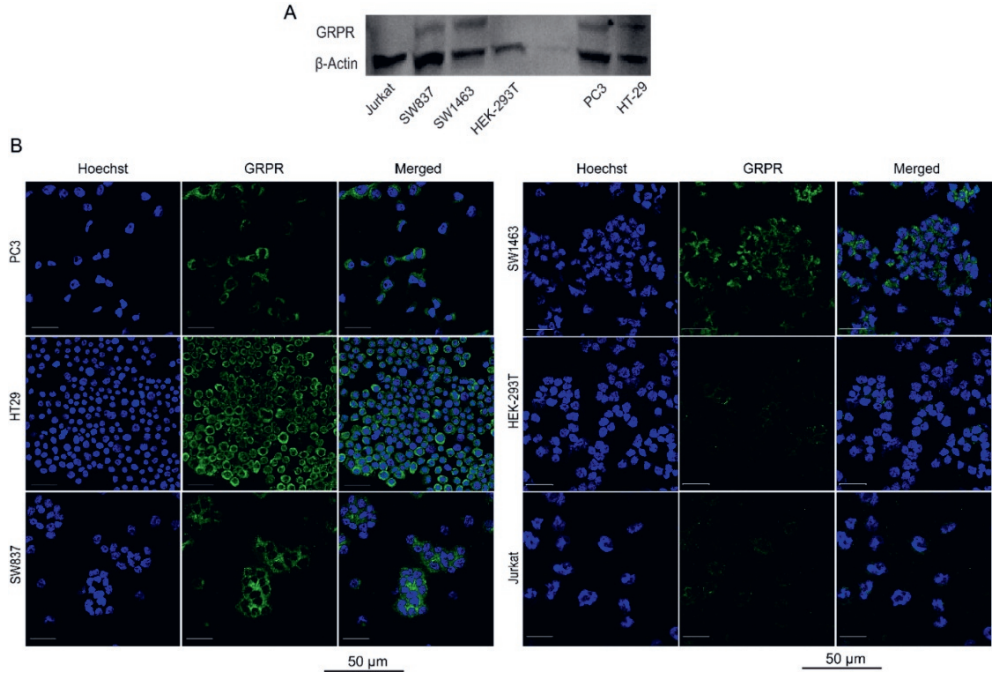

Figure 1. GRPR is upregulated in rectal cancer. (A) Western blot analysis confirmed GRPR expression in PC3, HT29, SW837, and SW1463 cell lines, while no expression was detected in HEK-293T and Jurkat cells. Actin was used as a loading control. Note: The slightly weaker β-Actin band in the HEK-293T group is due to minor loading variation (B) Immunofluorescence analysis showing the localization of GRPR (green) in PC3, HT29, SW837, SW1463, HEK-293T, and Jurkat cells, with nuclei stained with Hoechst 33342 (blue). Scale bars are indicated.

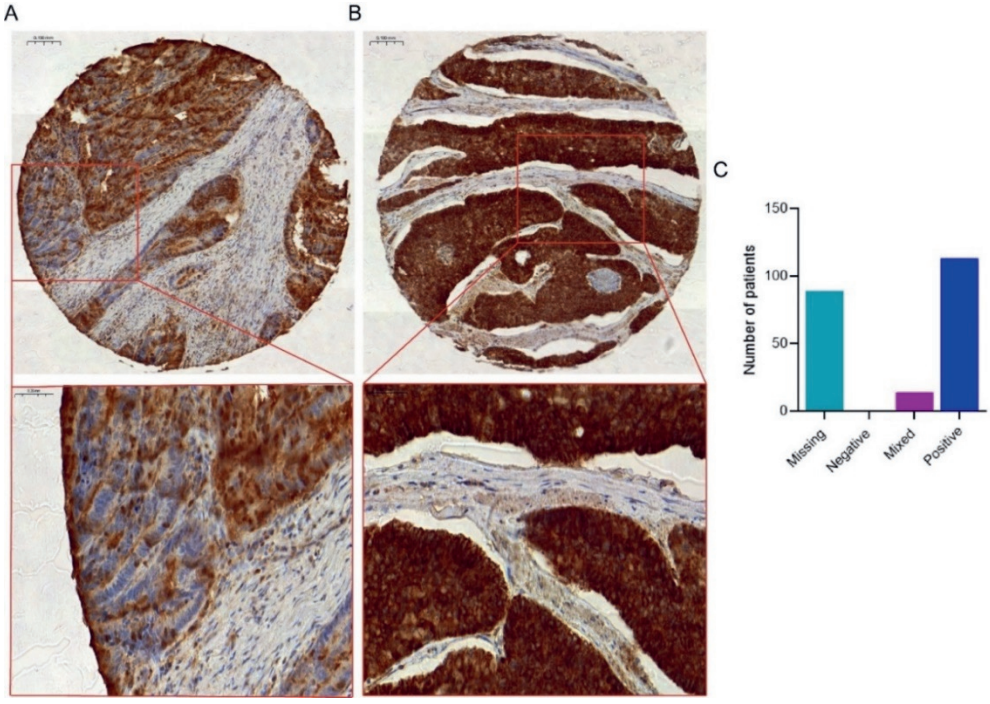

Figure 2. Representative images showing GRPR expression in rectal cancer tissue samples. GRPR expression was determined by immunohistochemical staining with GRPR showing in brown. Cases showed GRPR-negative cells next to GRPR-positive cells (A, indicated as mixed) or showed GRPR-expressing tumor cells only (B, indicated as positive). (C) Distribution of patients across both staining categories.

After investigating the expression of GRPR across several cancer cell lines, including PC3, HT29, SW837, SW1463, HEK-293T, and Jurkat, we developed a peptide, GRP-DP (Supplementary Figure 1), specifically designed to target GRPR-expressing cells. The peptide was engineered with an optimized sequence to enhance its binding affinity to GRPR. The modifications to the GRP-DP sequence were driven by two key objectives: improving stability, reducing degradation, and enhancing targeting efficiency, as well as increasing bioactivity and binding affinity [63]. First, Glu (Glutamic Acid) was removed to prevent degradation by proteolytic enzymes and avoid cross-linking with NPs, since Glu does not contribute to receptor binding. Methionine was replaced with Lysine to prevent oxidation and improve stability, while Lysine's amino group optimized peptide attachment to NPs. The addition of a second phenylalanine boosted hydrophobic interactions and π-π stacking, increasing binding affinity. Substituting histidine with glycine enhanced stability under varying pH and prevented unintended NPs-peptide coupling, ensuring specific attachment. These modifications collectively enhanced the peptide's stability, bioactivity, and targeting efficiency. To predict the binding affinity and binding poses of the designed GRP-DP, a docking analysis was performed.

Protein docking revealed the interaction between GRPR and GRP-DP

The novel peptide GRP-DP, with the sequence (Ac-Gln-Trp-Ala-Val-Gly-Phe-Gly-Phe-Lys-PEG-NH2), was designed to keep the human GRP peptide-binding interactions by keeping the homologous segment (Trp-Ala-Val-Gly) [64], while refraining from antagonizing the GRPR receptor by removing the His-Leu-Met segment [65]. By utilizing molecular docking simulations, we aimed to obtain early insights into whether the GRP-DP is predicted to exhibit a comparable or superior binding affinity to GRPR relative to the BNN/GRP. The docking simulations resulted in a mean GRP-DP affinity of -22.0 kcal/mol, a mean GRP/BBN affinity of -21.6 kcal/mol, a mean GRP affinity of -22.6 kcal/mol, and a mean GRP interface affinity of -19.7 kcal/mol (Table 1). The top-performing peptide conformer of all docked peptides is GRP-DP-09, with a mean affinity of -22.4 kcal/mol, a median affinity of -21.8 kcal/mol, and a top affinity of -24,6 kcal/mol. The top performing conformer of GRP/BBN was GRP/BBN-03, with a mean affinity of -21.7 kcal/mol, a median affinity of -21.5 kcal/mol, and a top affinity of -23.6 kcal/mol.

Table 1. The predicted mean, median, and top-performing ADCP-scores (kcal/mol) for GRPR-targeting ligands determined by AutoDock-CrankPep. GRP-DP-09 was the top-performing conformer of GRP-DP, and GRP/BBN-03 was the top-performing conformer of GRP/BBN. The mean and median ADCP-scores were derived from the top 5 evaluations of each conformer.

Ligand	Sequences	Mean affinity (kcal/mol)	Median affinity (kcal/mol)	Top affinity (kcal/mol)
GRP/BBN	Gln-Trp-Ala-Val-Gly-His-Leu-Met	-21.6	-21.4	-23,6
GRP-DP	Gln-Trp-Ala-Val-Gly-Phe-Gly-Phe	-22.0	-21.9	-24,6
GRP-DP -09	Gln-Trp-Ala-Val-Gly-Phe-Gly-Phe	-22.4	-21.8	-24,6
GRP/BBN-03	Gln-Trp-Ala-Val-Gly-His-Leu-Met	-21.7	-21.5	-23.6

Figure 3 shows a 2D interaction map of the top performing conformers of GRP-DP and GRP/BBN. The top performing GRP/BBN conformer, GRP/BBN-03, was not predicted to form any H-bonds. The top performing GRP-DP conformer, GRP-DP -09, was shown to be a hydrogen acceptor for the R283 and R308 sidechains, which increased the predicted binding affinity. Both GRP/BBN-03 and GRP-DP-09 were predicted to form a π-π interaction with F184 and their tryptophan amino acid, which indicates that W2 and F184 are important for generating poses that are predicted to be favorable. Furthermore, GRP/BBN-03 showed that a π-π interaction with Y101 was also important for gaining a favorable pose. This is in coherence with the Peng et al. paper [43], however the orientation of both GRP-DP-09 and

GRP/BBN-03 were flipped in the docking study, where W2 interacts with F184 and F193, while H6 interacts with Y101. The GRP-DP -09 C-terminus is exposed to the solvent, positioned in the opening of the binding cavity, which can be accessed for probe synthesis. GRP/BBN-03, the most favorable GRP/BBN pose, was shown to expose only the side group of V 4, which is not suitable for probe attachment.

Experimental validation of FITC@GRP-DP binding to GRPR

In addition to the docking study, we determined the binding affinity experimentally of the designed peptide FITC@GRP-DP using the FP assay. As shown in (Figure 3C), the FITC@GRP-DP was effectively bound to the GRPR protein. By varying the GRPR concentration, the dissociation constant (Kd) was determined, resulting in a calculated Kd of 4 µM based on the data.

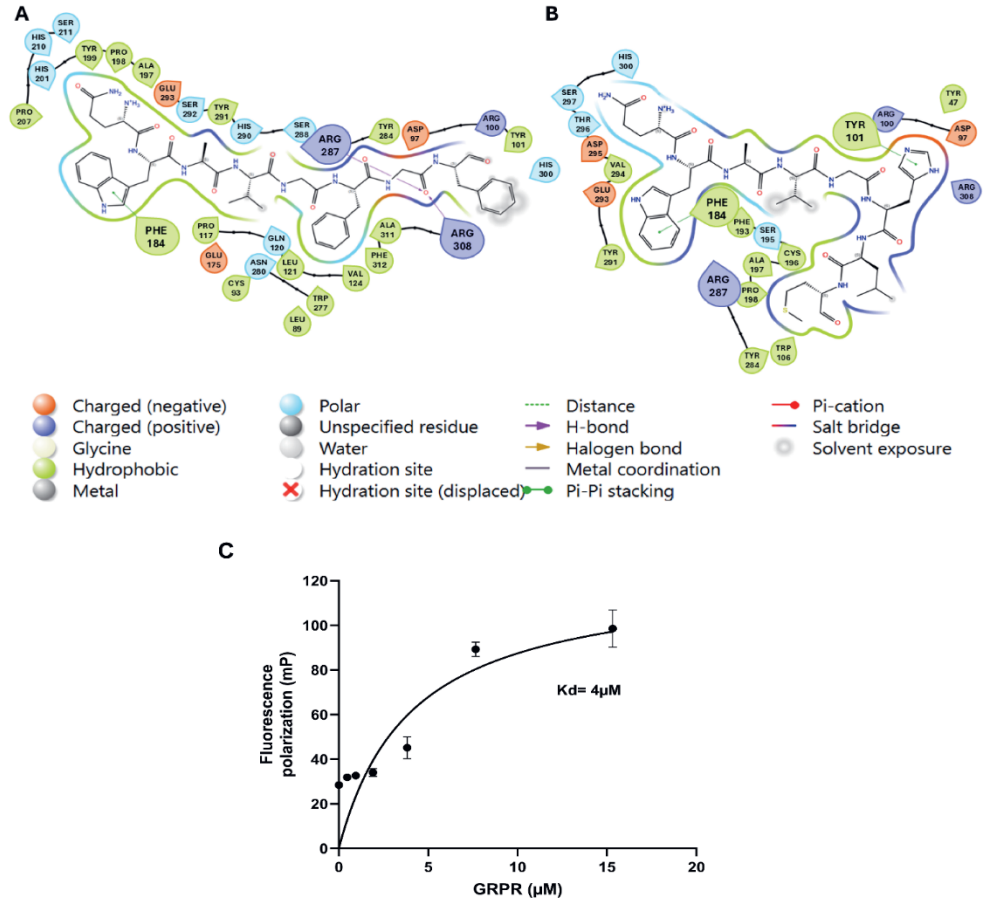

Figure 3. 2D interaction map of the peptides GRP-DP -09 and GRP/BBN-03. (A) GRP-DP -09's G7 amino acid side group is predicted to form a hydrogen bond interaction with the R287 and R308 residues of GRPR. Furthermore, W2 is shown to form π-π interactions with the hydrophobic F184, resulting in a

maintained pose and gain a favorable predicted binding affinity. The Q1 side group of GRP-DP -09 and N-terminus is relatively exposed to the solvent at the opening of the binding pocket. (B) GRP/BBN-03 does not seem to make any direct hydrogen bond interactions, however it seems to obtain a favorable pose due to the π-π interaction made with peptide amino acid H6 and protein amino acid Y101 and, just like GRP-DP -09, due to the π-π interaction W2 with F184. The side group of V4 was shown to be exposed to the solvent. (C) Fluorescence polarization (FP) saturation binding curves of FITC@GRP-DP at varying concentrations of GRPR protein. The curves illustrate the binding interaction between the FITC@GRP-DP ligand and GRPR, plotted as fluorescence polarization values (mP) versus GRPR protein concentration (μM). Data points represent the mean ± standard deviation (SD) of triplicate measurements.

Synthesis and Characterization of NPs

In addition to using FITC@GRP-DP as a probe for targeting GRPR in rectal cancer cells, we conjugated unlabeled GRP-DP to synthesize ICG-NPs, utilizing the NPs as an additional probe for targeted imaging. The NPs were characterized using DLS to measure particle size, zeta potential, and polydispersity index (PDI). The obtained data (Supplementary Table 1) revealed that the particle size of ICG-NPs was 139±0.94 nm with a negative surface charge of -14.7±0.15 mV. Upon conjugation with targeted peptides (Gn-RH and GRP-DP), the particle size and surface charge of the (ICG-NPs) were changed. The amount of ICG loaded in the ICG-NPs, GnRH@ICG-NPs and GRP-DP@ICG-NPs was measured as described in materials and methods (2.10.2). The percentage encapsulation efficiency (%EE) of ICG was determined to be 86.18± 1.4%, and the Loading capacity (LC) was found to be 4.52±0.08%. The morphology of the NPs was examined using TEM. The images revealed that the NPs exhibited a spherical shape with uniform sizes (Supplementary Figures 2A). Moreover ,ICG-NPs, GnRH@ICG-NPs and GRP-DP @ICG-NPs were imaged by fluorescence microscopy to confirm the successful encapsulation of ICG into a single NPs (Supplementary Figures 2B) [49].

The Gn-RH and GRP-DP targeting peptides were conjugated to the ICG/PLGA-PEG-2000-NHS NPs using NHS ester coupling. In this reaction, N-hydroxysuccinimide (NHS) ester groups present on the PLGA-PEG2000-NHS react with primary amines (NH_2 groups) on peptides to form stable amide bonds. This coupling reaction is widely used in bioconjugation and peptide chemistry for attaching peptides, proteins, or other molecules to various carriers or surfaces [66, 67]. Afterward, unconjugated peptides were removed through centrifugation processes to finally obtain the GnRH@ICG-NPs and GRP-DP@ICG-NPs. As a further step, we characterized the extent of this conjugation reaction using ^1H NMR, which allowed for obtaining the spectra for hydrogen nuclei specific for the ICG-NPs, the peptides (GRP-DP, GnRH), and the conjugate (GRP-DP@ICG-NPs, GnRH@ICG-NPs) as shown overlapped in (Supplementary Figures 3, 4) respectively. The peak at 3.6 ppm corresponds to the methylene protons ($-CH_2CH_2O-$) of PEG, representing the repeating ethylene glycol units in ICG-NPs. Additionally, two multiples are observed at 5.4 and 5.2 ppm, assigned to the protons ($CH-CH_3$) from lactic acid and (CH-H) from glycolic acid, respectively. A peak at 1.59 ppm indicates the methyl groups in the lactic acid repeats of ICG-NPs [68]. Moreover, the peak at 2.7 ppm corresponds to the NHS group of PEG-2000 in ICG-NPs [69]. In analyzing the GRP-DP sequence Ac-Gln-Trp-Ala-Val-Gly-Phe-Gly-Phe-Lys-PEG-NH_2, the ^1H NMR spectrum reveals distinctive peaks corresponding to various proton environments. The terminal NH_2 group from the PEG moiety is expected to resonate between 1 and

3 ppm. The amide protons in the peptide backbone, derived from the residues Gln, Trp, Ala, Val, Gly, Phe, and Lys, typically resonate in the 7 to 7.6 ppm range. Notably, the NH_2 protons of lysine were observed in the 7.6 to 8 ppm range [70]. The disappearance of the NHS heterocyclic peak at 2.7 ppm in the GRP-DP@ICG-NPs compared to ICG-NPs confirms the successful conjugation of GRP-DP to the NHS termini of ICG-NPs. In the ^1H NMR spectra of GRP-DP@ICG-NPs, signals between 7 and 7.6 ppm correspond to the amide protons (–NH) of the amino acids in GRP-DP. The absence of the NH_2 protons from lysine in GRP-DP@ICG-NPs further validates the conjugation. Additionally, new peaks observed at 6.5 and 8.5 ppm correspond to the amide protons formed during the conjugation, indicating the successful formation of the amide bond between GRP-DP and the ICG-NPs. The conjugation of the GnRH peptide to ICG-NPs was confirmed by the signals observed at around 6.6, 6.7, 7.0, and 7.2 ppm, which are attributed to the amide protons (–NH) in the peptide's amino acids, validating its attachment to the ICG-NPs (Supplementary Figure 4).

The maximal absorbance of free ICG in H_2O was observed around 780 nm, with a shoulder at 710 nm (Figure 4A). The intensity of ICG absorbance was directly proportional to its concentration in the aqueous solution. When ICG was encapsulated into ICG-NPs, the absorption maximum shifted slightly to longer wavelengths, peaking at approximately 800 nm with a shoulder at 730 nm (Figure 4C). Increased concentration of ICG in the ICG-NPs also led to increased absorbance (Figure 4B). Increasing the concentration of free ICG in the solution generally caused an increase in fluorescence (Figure 4D) However, at high concentrations, the self-quenching properties of ICG became evident (48 µg/mL) (Figure 4D). The self-quenching phenomenon of ICG loaded in PLGA NPs has been observed before, particularly when using the spontaneous emulsification solvent diffusion method [71]. In this study, increasing the concentration of ICG-NPs significantly enhanced the fluorescent signal. Moreover, the amount of ICG in 1000 µg/mL ICG-NPs did not exhibit self-quenching (Figure 4E). To further optimize ICG, we measured its release from PLGA-based NPs at physiological pH (7.4) over 192 h. ICG-NPs, GnRH@ICG-NPs, and GRP-DP@NPs were incubated in PBS at 37°C (Figure 4F). The data showed that ICG-NPs released about 80% of ICG at 24 h and 100% at 192 h. Targeted NPs (GnRH@ICG-NPs and GRP-DP@NPs) exhibited a sustained release, demonstrating the benefits of PLGA NPs in improving stability, sustained release, and enhanced targeting efficiency. The statistical analysis showed a highly significant difference (**** $p \leq 0.0001$) between the targeted and ICG-NPs in terms of ICG release (Figure 4F).

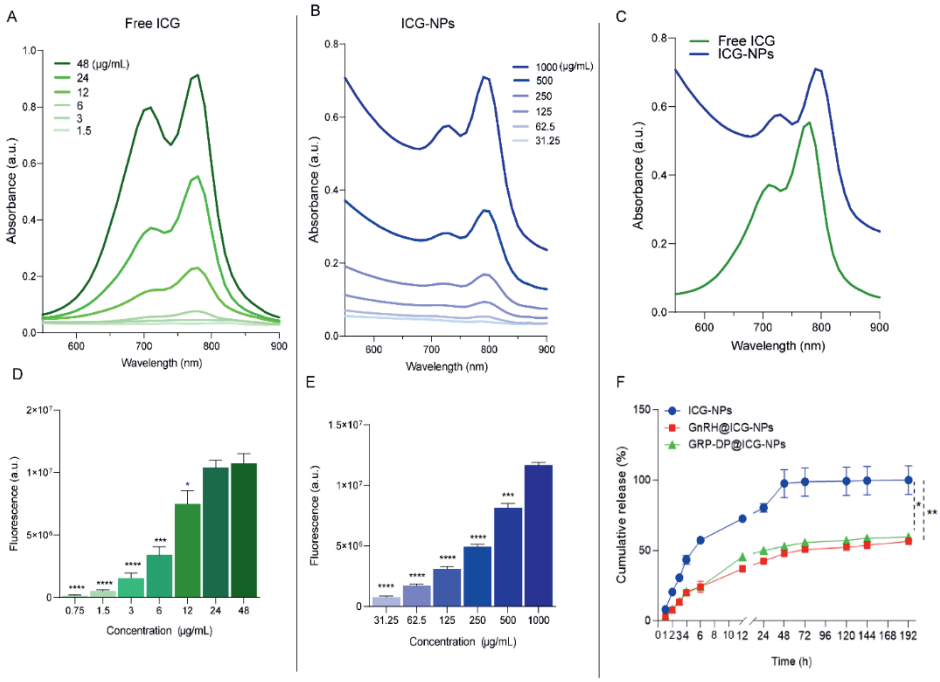

Figure 4. Optical properties and release profile of ICG and ICG-loaded NPs. (A–E) Absorbance and emission spectra of free ICG and ICG-NPs.(F) Cumulative release of ICG from ICG-NPs, GnRH@ICG-NPs, and GRP-DP@ICG-NPs over 192 hours in PBS (pH 7.4) at 37°C. Data are shown as mean ± SD (n = 3). Statistical significance is indicated as follows: *$p \leq 0.05$, **$p \leq 0.01$, ***$p \leq 0.001$, ****$p \leq 0.0001$.

Cellular experiment

After analyzing GRPR expression in various cell lines, we investigated the uptake and specificity of the GRPR-targeting peptide in live-cell imaging experiments. HT29, PC3, SW837, SW1463, and HEK-293T cells were incubated with FITC@GRP-DP and FITC@GRP-SP at 37°C, followed by fluorescence microscopy. Strong internalization of FITC@GRP-DP was observed in GRPR-positive HT29 and PC3 cells, confirming GRPR specificity (Figure 5A). In contrast, HEK-293T (GRPR-negative) cells exhibited minimal fluorescence, while SW837 and SW1463 cells showed moderate fluorescence. To assess the relationship between fluorescence intensity and peptide concentration, we tested 2.5 μM, 10 μM, and 20 μM FITC@GRP-DP in these cell lines. Fluorescence intensity increased in a concentration-dependent manner, particularly in HT29 and PC3, with smaller increases in SW837 and SW1463, while HEK-293T remained negligible (Figure 5A). These findings further confirm the specificity and uptake efficiency of FITC@GRP-DP in GRPR-expressing cells. Similarly, the FITC@GRP-SP probe, was incubated with GRPR-positive cell lines (PC3) at concentrations of 2.5, 10, and 20 μM under the same conditions as FITC@GRP-DP. Fluorescence imaging showed no detectable uptake or binding of FITC@SP in HT29 and PC3 cells, confirming its absence of specific interaction (Figure 5B).

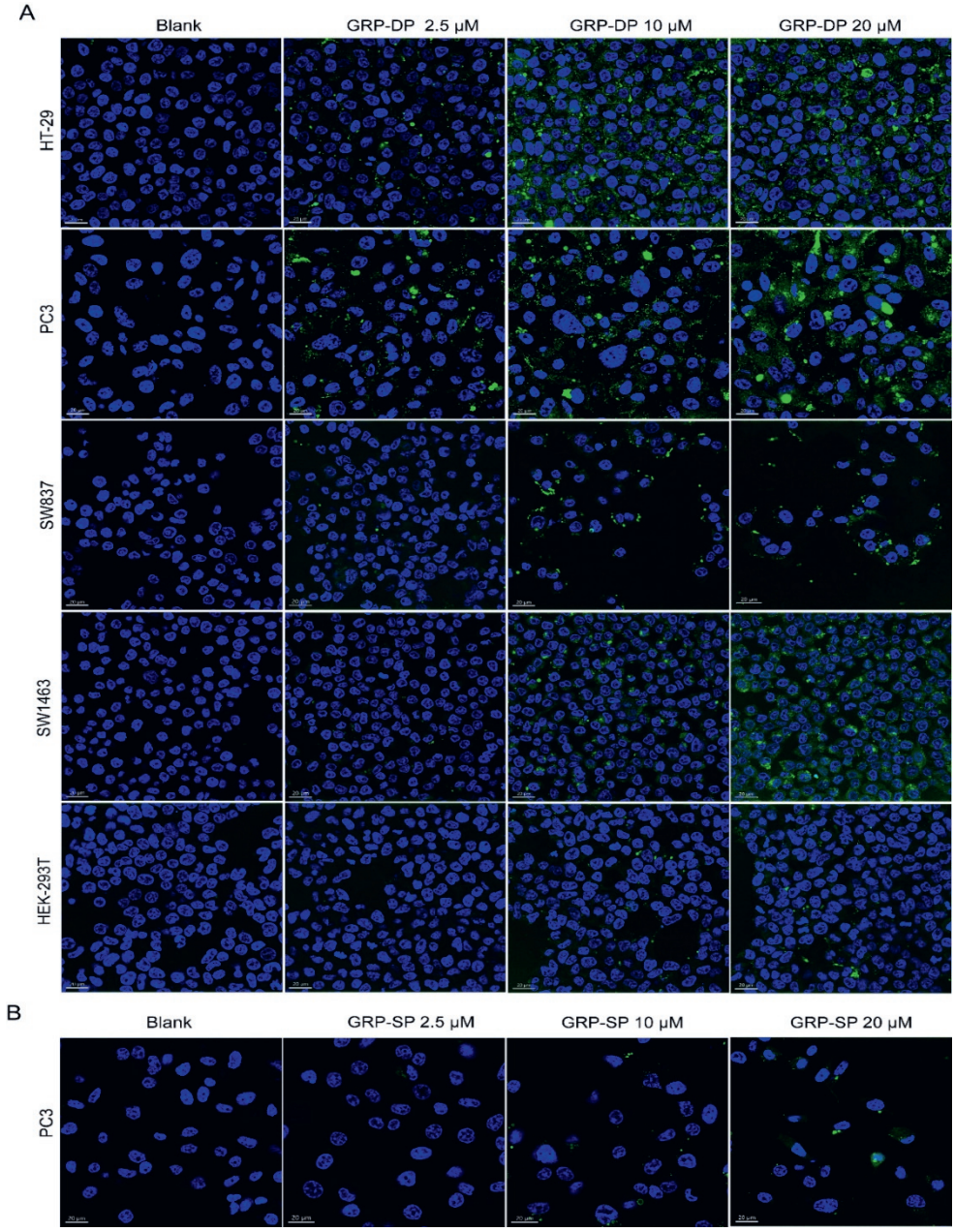

Figure 5. Live-Cell Imaging of FITC@GRP-DP and FITC@GRP-SP Binding to GRPR-Positive and GRPR-Negative Cells (A) Fluorescence microscopy images show Hoechst 33342-stained nuclei (blue) and FITC@GRP-DP fluorescence (green). HT29, PC3, SW837, and SW1463 cells exhibit progressively enhanced membrane fluorescence with increasing FITC@GRP-DP concentrations (2.5, 10, and 20 μM),

while HEK-293T cells display minimal signal, confirming selective binding to GRPR-positive cells at 37°C. (B) PC3 cells incubated with FITC@GRP-SP under identical conditions exhibit negligible fluorescence, suggesting a lack of GRPR affinity.

In parallel with the FITC@GRP-DP probe, we studied ICG-NPs exclusively in rectal cancer cells to develop a targeting vehicle for NIR imaging. To investigate this, we first examined cell viability by increasing the concentration of NPs, which also raised the ICG concentration loaded in the NPs, to assess their effect on rectal cancer cells. Rectal cancer cell lines SW837 and SW1463 were incubated with various concentrations of ICG-NPs, GnRH@ICG-NPs, and GRP-DP@ICG-NPs. The cytotoxic effects of the NPs on cell viability were measured using the MTS assay. The results showed no significant changes in cell viability for SW837 and SW1463 cells over the 72 h period (data not shown), indicating that the delivery of ICG via these NPs did not reduce the viability of rectal cancer cells. As shown in (Supplementary Figure 5), fluorescence intensity in SW837 cells increased over time for all ICG-NP formulations. GRP-DP@ICG-NPs exhibited higher uptake than ICG-NPs at all time points, while GnRH@ICG-NPs showed significantly greater uptake than ICG-NPs only at 4 and 8 h. These findings suggest that GRP-DP@ICG-NPs maintain superior uptake efficiency throughout the study, whereas GnRH@ICG-NPs demonstrate enhanced uptake primarily at later time points. Among the NP formulations, GRP-DP@ICG-NPs exhibited significantly higher fluorescent intensity compared to GnRH@ICG-NPs in SW837 cells (*$P \leq 0.05$, **$P \leq 0.01$, ***$P \leq 0.001$, ****$P \leq 0.0001$). A similar pattern was observed in SW1463 cells (data not shown). Fluorescence microscopy was used to visualize ICG-NP, GnRH@ICG-NP, and GRP-DP@ICG-NP uptake and localization in SW837 cells at 2, 4, and 8 h, highlighting the influence of size, PDI, surface charge, and modifications on uptake . As reported previously, all ICG-NPs, GnRH@ICG-NPs, and GRP-DP@ICG-NPs were negatively charged, and there was no significant difference between their sizes. The only important difference was the surface modification by targeting peptides. The Non-targeted ICG-NPs rely on passive endocytosis mechanisms and are generally less specific, but they still provided a means of ICG delivery by increasing fluorescence intensity over the 8 h period. In contrast, GRP-DP@ICG-NPs exhibit enhanced selectivity and efficiency for SW837 cells due to receptor-ligand interactions (Supplementary Figure 6).

4. Discussion

GRPR is found in significantly high levels on colorectal cancer cells, making it an excellent biomarker for molecular targeting and diagnosing CRC [58]. Its selective presence on cancerous cells, while absent in normal epithelium, is increasingly documented in the literature [72]. Additionally, studies on GRPR expression in colon cancer have shown a strong correlation with tumor differentiation. GRPR is highly expressed in well-differentiated tumors, intermediate in moderately differentiated ones, and minimal or absent in poorly differentiated cancers. This suggests a role in maintaining tumor differentiation and influencing clinical outcomes. Higher GRPR expression is linked to improved survival and delayed recurrence, likely due to its role in cellular adhesion, tumor stabilization, and reduced metastasis [73-75].

In this study, we present the first evaluation of GRPR expression in rectal cancer at both the cellular and tissue levels, providing evidence that human rectal cancer cells express GRPR binding sites. Afterward, we designed FITC-labeled GRP-DP and GRP-DP@ICG-NPs as probes for targeting GRPR**.** The

designed novel GRP-DP was strategically engineered to maintain its biological binding properties. GRP-DP was modified based on a study by Durkan et al., using radiolabeled Litorin (pGlu-Gln-Trp-Ala-Val-Gly-His-Phe-Met-NH2), a peptide similar to BBN. In vitro studies indicate that 99mTc-litorin has high serum stability, while *in vivo* tests in rats show rapid clearance and specific uptake in BN/GRP receptor-rich tissues like the pancreas. This highlights its potential as a radiopharmaceutical for detecting cancers that express bombesin receptors [63]. The docking data suggest that GRP-DP exhibits a binding affinity comparable to that of GRP and GRP/BBN. Importantly, GRP-DP effectively bound to the GRPR, with its binding affinity (Kd) in our study falling within the micromolar range. This finding highlights the potential of GRP-DP for targeted applications involving GRPR. Previous studies have demonstrated the binding affinities of GRP and BBN for wild-type GRPR expressed in BALB 3T3 cells. BBN and GRP, which are naturally occurring agonists related to the bombesin family, exhibit high affinity for GRPR, with an IC50 of 2.7 nM [76]. Additionally, another study evaluated the binding affinity of BBN7–14 and GB-6 peptides at a cellular level using CFPAC-1 cells (high GRPR expression) and HeLa cells (minimal GRPR expression) [13]. The reported apparent dissociation constants (Kd) were 1.5 μM for BBN7–14-FITC and 3.1 μM for GB-6-FITC. Furthermore, Yuze Ma et al. reviewed the binding affinity and capacity of radiolabeled GRPR ligands for PET/CT imaging across various cancers [10]. Radiolabeled GRPR ligands demonstrate varying binding affinities and capacities, with antagonists generally outperforming agonists in imaging efficiency and safety. These ligands have shown promise in GRPR-positive cancers, especially prostate and breast cancers, by offering high tumor-specific uptake and reducing off-target effects. [10]. Near-infrared fluorescence using ICG provides real-time intraoperative guidance in colorectal surgery, aiding tissue perfusion assessment and reducing complications like anastomotic leakage. However, the tendency of ICG to aggregate and its lack of tumor specificity limit its effectiveness. Encapsulation in PLGA NPs stabilizes ICG, prevents aggregation, and extends its circulation half-life for improved imaging and therapy [7, 26, 71, 77-80].

In the present study, we encapsulated ICG within PLGA-PEG NPs and focused on characterizing the biological behavior of both ICG-NPs and peptide-targeted ICG-NPs. The primary components, including ICG, PLGA, and peptides, are FDA-approved and have been widely used in various medical applications [81]. In previous studies, ICG was encapsulated in PLGA NPs [57, 82], but without achieving the level of specificity we present here. Additionally, those studies did not focus on rectal cancer. We synthesized PLGA NPs and modified their surface with PEG (PEGylation) to enhance circulation time and reduce liver and spleen accumulation [83]. The UV-Vis fluorescence spectra of free ICG and ICG-loaded PLGA NPs have shown variability across studies. While some report no spectral shift upon encapsulation [21, 84, 85], others observe a shift in peak fluorescence from 807 to 813 nm, likely due to self-quenching or molecular aggregation [86]. Using an oil/water emulsion and solvent evaporation-extraction method, we incorporated ICG into PLGA-PEG NPs, observing no significant shift in absorbance or emission wavelengths compared to free ICG. The aim of incorporating ICG into PLGA-PEG NPs and targeting them with DP-GRP was to develop a stable, long-circulating fluorescent probe for imaging and targeting GRPR-positive rectal tumors. Currently, few fluorescent probes are available for GRPR imaging. For example, a series of NIR fluorescent probes linked to a GRPR antagonist have been developed, demonstrating high affinity and selectivity for prostate cancer in both in vitro and in vivo studies [62]. However, small-molecule-based fluorescent probes often face limitations such as poor photostability, small stokes shifts, and short fluorescence lifetimes. Additionally, developing GRPR probes with adequate biocompatibility to effectively study

their roles in proliferation and inflammation remains a significant challenge [62]. Delivering peptide tracers to their target site is challenging due to the presence of proteolytic enzymes in the blood, vascular walls, liver, lungs, kidneys, and gastrointestinal tract. Consequently, these enzymes can degrade the peptide tracers, which may hinder their targeting properties and limit their effectiveness as theranostic probes [13]. To enhance the attachment of GRP-DP peptide to ICG-NP surfaces, modifications were implemented, leading to improved stability and bioactivity. These enhancements facilitated effective targeting of tumor cells. Prior studies have demonstrated that functionalizing NPs with peptides not only increases their uptake in tumor tissues but also enhances their ability to penetrate deeply and specifically target tumor vasculature, thus maximizing their potential in cancer imaging and therapy [87, 88]. In this study, we investigate the utilization of the GRP-DP, both as a standalone and in conjunction ICG-NPs, to enhance cellular uptake. The cellular experiments with FITC-labeled GRP-DP and GRP-DP@ICG-NPs demonstrated effective targeting of GRPR-positive rectal cancer cells using these probes for image-guided surgery. However, a notable distinction existed between the use of FITC-labeled GRP-DP alone and GRP-DP@ICG-NPs for imaging. While FITC-labeled GRP-DP functioned as a simple fluorescence-based probe, GRP-DP@ICG-NPs enhanced imaging capabilities by integrating fluorescence with NIR imaging, which provided superior tissue penetration and potentially more precise tumor localization during image-guided surgery.

Conclusion

In summary, this study examined GRPR expression in rectal cancer at both the cellular and tissue levels, confirming its potential as a biomarker for targeted imaging. Furthermore, the novel GRP-DP peptide enhanced the specificity of GRPR-targeted imaging in rectal cancer. By encapsulating ICG in PLGA-PEG NPs, we developed an effective strategy for improving intraoperative tumor visualization and surgical precision. This approach may not only improve the stability and circulation time of ICG but also enable targeted delivery to GRPR-overexpressing rectal cancer cells. The findings emphasize the potential of integrating peptide-functionalized NPs loaded with ICG for enhanced tumor imaging offering a promising avenue for better rectal cancer management and improved surgical outcomes.

Targeting Rectal Cancer Using Fluorescent Nanoparticles Conjugated to a Novel GRPR-Binding Peptide for Tumor Imaging Applications

Somayeh Rezaei, Mark Fonteyne, Luis J. Cruz, Nada Badr, Ajinkya Manelkar, Mahin Saberi, Ronald L.P. van Vlierberghe, Alexander L. Vahrmeijer, Christina Eich, Fernando Albericio, Louise van der Weerd, and Peter J.K. Kuppen.

Materials & Design.

Supplementary Material

Supplementary Figure 1. Chemical structure of the GRP-DP ligand (Ac-Gln-Trp-Ala-Val-Gly-Phe-Gly-Phe-Lys-PEG-NH2).

Supplementary Figures 2. Morphology and representative images of NPs. (A) Transmission electron microscopy (TEM) images of ICG-NPs, GRP-DP@ICG-NPs, and GnRH@ICG-NPs, illustrating particle morphology (scale bar: 100 nm). (B) Fluorescence microscopy images of the same NPs, showing ICG fluorescence (green). The NPs were dissolved in water and coated onto glass coverslips (scale bar: 20 µm,).

Supplementary Figures 3. ^{1}H NMR characterization of GRP-DP, ICG-NPs, and GRP-DP@ICG-NPs conjugation. Overlapped spectra with coinciding regions are shown in panels (A) and (B) (850 MHz, D_2O).

Supplementary Figure 4. ^{1}H NMR characterization of GnRH peptide, ICG-NPs, and GnRH@ICG-NPs conjugation (850 MHz, D_2O).

Supplementary Figure 5. Uptake assay of NPs in SW837 cells using the odyssey assay. SW837 cells were incubated with ICG-NPs, GnRH@ICG-NPs, and GRP-DP@ICG-NPs for 1, 2, 4, and 8 h. Uptake was analyzed by calculating fluorescence intensity as the ratio of the signal at 800 nm (ICG) to 700 nm (nucleus stained with TO-PRO®-3). Data are shown as mean ± SD (n = 3). Statistical significance: *$p \leq 0.05$, **$p \leq 0.01$, ***$p \leq 0.001$, ****$p \leq 0.0001$.

Supplementary Figure 6. Uptake and intracellular distribution of ICG-NPs in SW837 cells**.** Representative fluorescence microscopy images show SW837 cells incubated with ICG-NPs, GnRH@ICG-NPs, and GRP-DP@ICG-NPs for 4 h (A) and 8 h (B). Nuclei are stained with DAPI (blue), and ICG fluorescence is depicted in purple. Images were captured and analyzed using fluorescence microscopy. Scale bar: 50 µm.

Supplementary Table 1. Physicochemical Characterization of Nanoparticles by Dynamic Light Scattering (DLS).

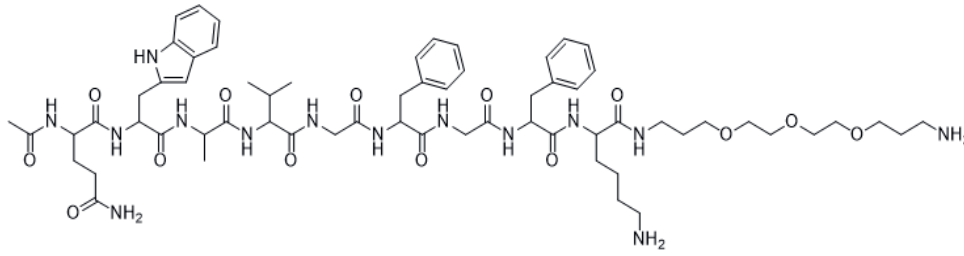

Supplementary Figure 1. Chemical structure of the GRP-DP ligand (Ac-Gln-Trp-Ala-Val-Gly-Phe-Gly-Phe-Lys-PEG-NH2).

Supplementary Table 1. Physicochemical Characterization of Nanoparticles by Dynamic Light Scattering (DLS).

NPs	Size (nm)	ζpotential (mV)	PDI
ICG-NPs	139± 0.94	-14.7± 0.15	0.123±0.02
GnRH@ICG-NPs	145± 1.65	-18.2± 0.88	0.102±0.02
GRP-DP@ICG-NPs	149± 2.68	-16.3± 0.10	0.121±0.004

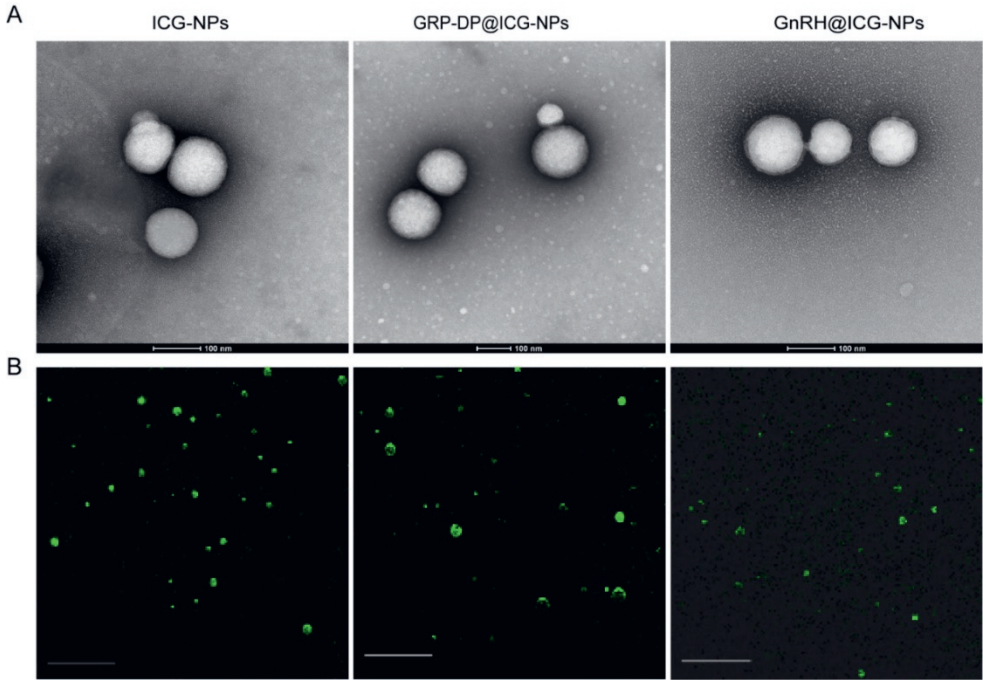

Supplementary Figures 2. Morphology and representative images of NPs. (A) Transmission electron microscopy (TEM) images of ICG-NPs, GRP-DP@ICG-NPs, and GnRH@ICG-NPs, illustrating particle morphology (scale bar: 100 nm). (B) Fluorescence microscopy images of the same NPs, showing ICG fluorescence (green). The NPs were dissolved in water and coated onto glass coverslips (scale bar: 20 µm,).

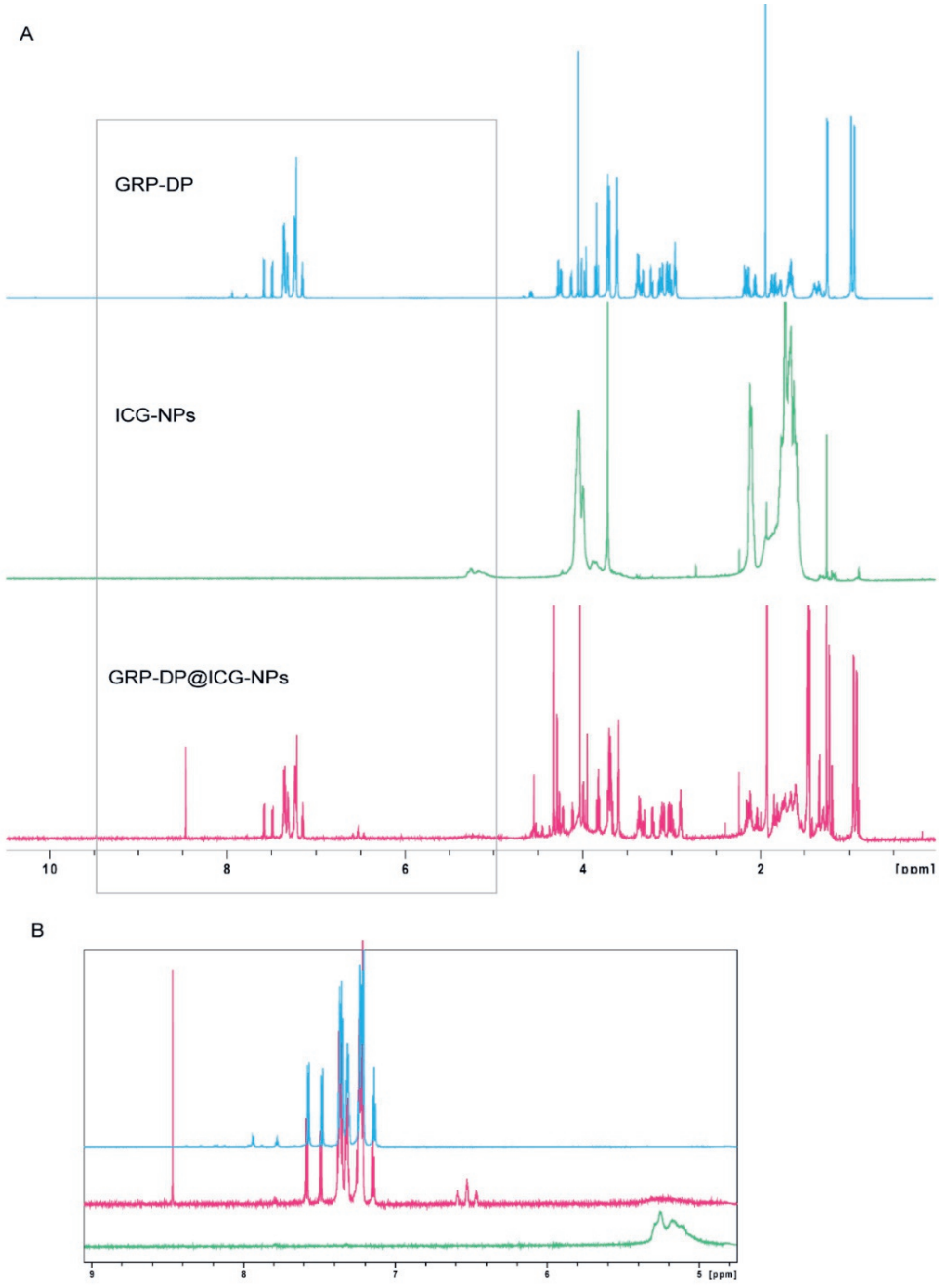

Supplementary Figures 3. ^{1}H NMR characterization of GRP-DP, ICG-NPs, and GRP-DP@ICG-NPs conjugation. Overlapped spectra with coinciding regions are shown in panels (A) and (B) (850 MHz, D_2O).

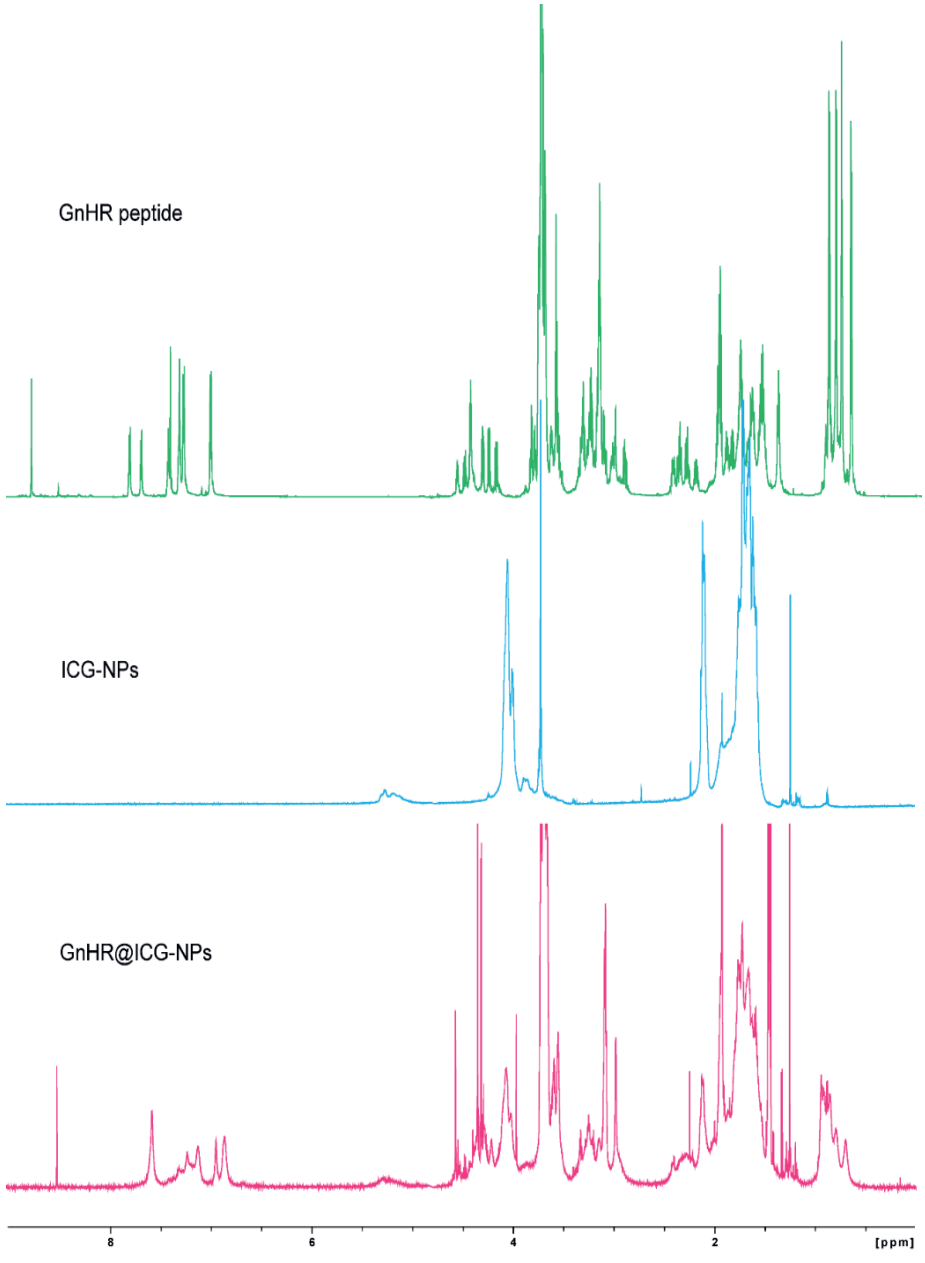

Supplementary Figure 4. ^{1}H NMR characterization of GnRH peptide, ICG-NPs, and GnRH@ICG-NPs conjugation (850 MHz, D_2O).

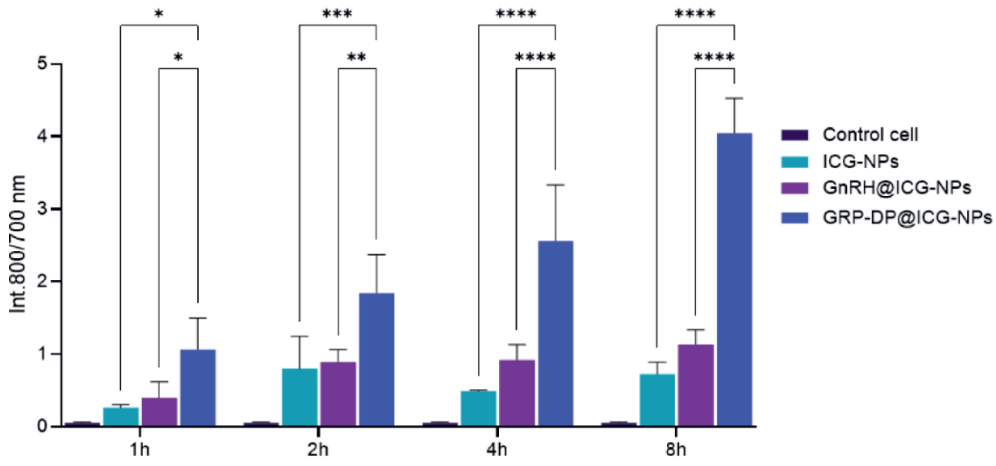

Supplementary Figure 5. Uptake assay of NPs in SW837 cells using the odyssey assay. SW837 cells were incubated with ICG-NPs, GnRH@ICG-NPs, and GRP-DP@ICG-NPs for 1, 2, 4, and 8 h. Uptake was analyzed by calculating fluorescence intensity as the ratio of the signal at 800 nm (ICG) to 700 nm (nucleus stained with TO-PRO®-3). Data are shown as mean ± SD (n = 3). Statistical significance: *$p \leq 0.05$, **$p \leq 0.01$, ***$p \leq 0.001$, ****$p \leq 0.0001$.

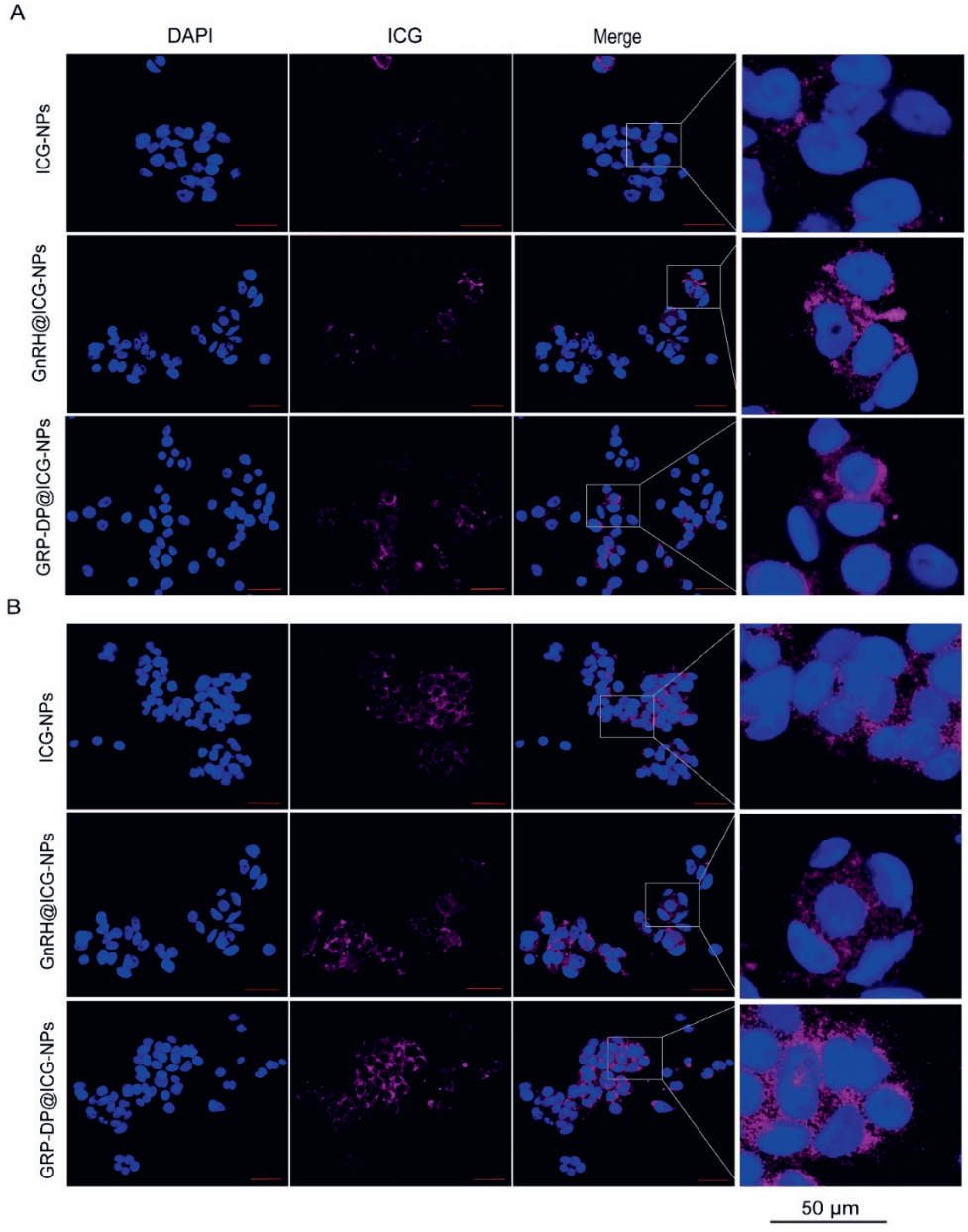

Supplementary Figure 6. Uptake and intracellular distribution of ICG-NPs in SW837 cells**.** Representative fluorescence microscopy images show SW837 cells incubated with ICG-NPs, GnRH@ICG-NPs, and GRP-DP@ICG-NPs for 4 h (A) and 8 h (B). Nuclei are stained with DAPI (blue), and ICG fluorescence is depicted in purple. Images were captured and analyzed using fluorescence microscopy. Scale bar: 50 μm.

References

[1] J. Shen, S. Lu, R. Qu, H. Zhao, Y. Zhang, A. Chang, L. Zhang, W. Fu, Z. Zhang, Measuring distance from lowest boundary of rectal tumor to anal verge on CT images using pyramid attention pooling transformer, Computers in Biology and Medicine 155 (2023) 106675.

[2] F. Fang, X. Zhang, J. Tang, Y. Wang, J. Xu, Y. Sun, EGFR-Targeted Hybrid Lipid Nanoparticles for Chemo-Photothermal Therapy Against Colorectal Cancer Cells, Chemistry and Physics of Lipids (2023) 105280.

[3] Z. Yin, C. Yao, L. Zhang, S. Qi, Application of artificial intelligence in diagnosis and treatment of colorectal cancer: A novel Prospect, Frontiers in Medicine 10 (2023).

[4] W. Deng, K.J. McKelvey, A. Guller, A. Fayzullin, J.M. Campbell, S. Clement, A. Habibalahi, Z. Wargocka, L. Liang, C. Shen, Application of mitochondrially targeted nanoconstructs to neoadjuvant x-ray-induced photodynamic therapy for rectal cancer, ACS central science 6(5) (2020) 715-726.

[5] D. Wolford, L. Westcott, J. Fleshman, Specialization improves outcomes in rectal cancer surgery, Surgical Oncology 43 (2022) 101740.

[6] D. Ribero, F. Mento, V. Sega, D. Lo Conte, A. Mellano, G. Spinoglio, ICG-Guided Lymphadenectomy during Surgery for Colon and Rectal Cancer—Interim Analysis of the GREENLIGHT Trial, Biomedicines 10(3) (2022) 541.

[7] P.A. Sutton, M.A. van Dam, R.A. Cahill, S. Mieog, K. Polom, A.L. Vahrmeijer, J. van der Vorst, Fluorescence-guided surgery: comprehensive review, BJS open 7(3) (2023) zrad049.

[8] M. Gao, F. Yu, C. Lv, J. Choo, L. Chen, Fluorescent chemical probes for accurate tumor diagnosis and targeting therapy, Chemical Society Reviews 46(8) (2017) 2237-2271.

[9] B.P. Rurarz, M. Bukowczyk, N. Gibka, A.W. Piastowska-Ciesielska, U. Karczmarczyk, P. Ulański, Nanostrategies for Therapeutic and Diagnostic Targeting of Gastrin-Releasing Peptide Receptor, International Journal of Molecular Sciences 24(4) (2023) 3455.

[10] Y. Ma, F. Gao, Advances of radiolabeled GRPR ligands for PET/CT imaging of cancers, Cancer Imaging 24(1) (2024) 19.

[11] X. Wen, R. Wang, P. Xu, M. Shi, Q. Shang, X. Zeng, X. Zeng, J. Liu, X. Wang, Z. Zhu, Synthesis, preclinical, and initial clinical evaluation of integrin αVβ3 and gastrin-releasing peptide receptor (GRPR) dual-targeting radiotracer [68Ga] Ga-RGD-RM26-03, European Journal of Nuclear Medicine and Molecular Imaging (2024) 1-13.

[12] A. Ramírez-Perdomo, G. Márquez-Barrios, L. Gutiérrez, R. Parra-Medina, Neuroendocrine Peptides in the pathogenesis of colorectal carcinoma, Experimental Oncology 45(1) (2023) 3-16.

[13] Y. Tu, J. Tao, F. Wang, P. Liu, Z. Han, Z. Li, Y. Ma, Y. Gu, A novel peptide targeting gastrin releasing peptide receptor for pancreatic neoplasm detection, Biomaterials science 8(9) (2020) 2682-2693.

[14] Q.Y. Cai, P. Yu, C. Besch‐Williford, C.J. Smith, G.L. Sieckman, T.J. Hoffman, L. Ma, Near‐infrared fluorescence imaging of gastrin releasing peptide receptor targeting in prostate cancer lymph node metastases, The Prostate 73(8) (2013) 842-854.

[15] H. Xu, R.P. Bandari, L. Lee, R. Li, P. Yu, C.J. Smith, L. Ma, Design, synthesis, and in vitro and in vivo evaluation of high affinity and specificity near-infrared fluorescent bombesin antagonists for tumor imaging, Journal of Medicinal Chemistry 61(17) (2018) 7657-7670.

[16] A. Pagoto, F. Garello, G.M. Marini, M. Tripepi, F. Arena, P. Bardini, R. Stefania, S. Lanzardo, G. Valbusa, F. Porpiglia, Novel gastrin-releasing peptide receptor targeted near-infrared fluorescence dye for image-guided surgery of prostate cancer, Molecular Imaging and Biology 22 (2020) 85-93.

[17] M. Sevieri, F. Silva, A. Bonizzi, L. Sitia, M. Truffi, S. Mazzucchelli, F. Corsi, Indocyanine green nanoparticles: Are they compelling for cancer treatment?, Frontiers in chemistry 8 (2020) 535.

[18] H. Li, X. Xie, F. Du, X. Zhu, H. Ren, C. Ye, Z. Liu, Y. Zhao, X. Yu, C. Zhang, A narrative review of intraoperative use of indocyanine green fluorescence imaging in gastrointestinal cancer: situation and future directions, Journal of Gastrointestinal Oncology 14(2) (2023) 1095.

[19] S. Ryu, K. Suwa, T. Kitagawa, M. Aizawa, T. Ushigome, T. Okamoto, K. Eto, K. Yanaga, Real-time fluorescence vessel navigation using indocyanine green during laparoscopic colorectal cancer surgery, Anticancer Research 39(6) (2019) 3009-3013.
[20] K. Safiejko, R. Tarkowski, T.P. Kozlowski, M. Koselak, M. Jachimiuk, A. Tarasik, M. Pruc, J. Smereka, L. Szarpak, Safety and efficacy of indocyanine green in colorectal cancer surgery: a systematic review and meta-analysis of 11,047 patients, Cancers 14(4) (2022) 1036.
[21] S. Choi, S.-H. Lee, S. Park, S.H. Park, C. Park, J. Key, Indocyanine green-loaded plga nanoparticles conjugated with hyaluronic acid improve target specificity in cervical cancer tumors, Yonsei Medical Journal 62(11) (2021) 1042.
[22] E. Belloni, E.M. Muttillo, S. Di Saverio, M. Gasparrini, A. Brescia, G. Nigri, The role of indocyanine green fluorescence in rectal cancer robotic surgery: a narrative review, Cancers 14(10) (2022) 2411.
[23] H. Abdelrahman, A. El-Menyar, R. Peralta, H. Al-Thani, Application of indocyanine green in surgery: A review of current evidence and implementation in trauma patients, World Journal of Gastrointestinal Surgery 15(5) (2023) 757-775.
[24] A. Obinu, E. Gavini, G. Rassu, F. Riva, A. Calligaro, M.C. Bonferoni, M. Maestri, P. Giunchedi, Indocyanine green loaded polymeric nanoparticles: Physicochemical characterization and interaction studies with Caco-2 cell line by light and transmission electron microscopy, Nanomaterials 10(1) (2020) 133.
[25] D. Miele, M. Sorrenti, L. Catenacci, P. Minzioni, G. Marrubini, V. Amendola, M. Maestri, P. Giunchedi, M.C. Bonferoni, Association of Indocyanine Green with Chitosan Oleate Coated PLGA Nanoparticles for Photodynamic Therapy, Pharmaceutics 14(8) (2022) 1740.
[26] C. Egloff-Juras, L. Bezdetnaya, G. Dolivet, H.-P. Lassalle, NIR fluorescence-guided tumor surgery: new strategies for the use of indocyanine green, International journal of nanomedicine (2019) 7823-7838.
[27] J. Park, Y. Pei, H. Hyun, M.A. Castanares, D.S. Collins, Y. Yeo, Small molecule delivery to solid tumors with chitosan-coated PLGA particles: A lesson learned from comparative imaging, Journal of Controlled Release 268 (2017) 407-415.
[28] J. Ghitman, E.I. Biru, R. Stan, H. Iovu, Review of hybrid PLGA nanoparticles: Future of smart drug delivery and theranostics medicine, Materials & Design 193 (2020) 108805.
[29] R. Mahar, A. Chakraborty, N. Nainwal, R. Bahuguna, M. Sajwan, V. Jakhmola, Application of PLGA as a Biodegradable and Biocompatible Polymer for Pulmonary Delivery of Drugs, AAPS PharmSciTech 24(1) (2023) 39.
[30] X. Shen, T. Li, X. Xie, Y. Feng, Z. Chen, H. Yang, C. Wu, S. Deng, Y. Liu, PLGA-based drug delivery systems for remotely triggered cancer therapeutic and diagnostic applications, Frontiers in Bioengineering and Biotechnology 8 (2020) 381.
[31] C. Conte, G. Longobardi, A. Barbieri, G. Palma, A. Luciano, G. Dal Poggetto, C. Avitabile, A. Pecoraro, A. Russo, G. Russo, Non-covalent strategies to functionalize polymeric nanoparticles with NGR peptides for targeting breast cancer, International Journal of Pharmaceutics (2023) 122618.
[32] V. Le Joncour, P. Laakkonen, Seek & Destroy, use of targeting peptides for cancer detection and drug delivery, Bioorganic & medicinal chemistry 26(10) (2018) 2797-2806.
[33] S. Khan, F. Mejia, J. Shin, G. Hwang, D.T. Omstead, J. Wu, S.L. Cole, L.E. Littlepage, B. Bilgicer, Disease-driven engineering of peptide-targeted DM1 loaded liposomal nanoparticles for enhanced efficacy in treating multiple myeloma by exploring DM1 prodrug chemistry, Biomaterials 292 (2023) 121913.
[34] G.G. Kordopati, T.V. Tselios, T. Kellici, F. Merzel, T. Mavromoustakos, S.G. Grdadolnik, G.M. Tsivgoulis, A novel synthetic luteinizing hormone-releasing hormone (LHRH) analogue coupled with modified β-cyclodextrin: Insight into its intramolecular interactions, Biochimica et Biophysica Acta (BBA)-General Subjects 1850(1) (2015) 159-168.
[35] F. Haviv, T.D. Fitzpatrick, Synthetic Approaches to Incorporation of Novel Amino Acids into Gonadotropin-Releasing Hormone Peptides, Methods in Neurosciences, Elsevier1993, pp. 3-18.

[36] I. Qamar, S. Rehman, G. Mehdi, V. Maheshwari, H.A. Ansari, S. Chauhan, Utility of cytospin and cell block technology in evaluation of body fluids and urine samples: A comparative study, Journal of cytology 35(2) (2018) 79.
[37] I. Larionova, A. Kiselev, E. Kazakova, T. Liu, M. Patysheva, P. Iamshchikov, Q. Liu, D.M. Mossel, V. Riabov, M. Rakina, Tumor-associated macrophages respond to chemotherapy by detrimental transcriptional reprogramming and suppressing stabilin-1 mediated clearance of EGF, Frontiers in Immunology 14 (2023).
[38] K.W. Kim, P. Paul, J. Qiao, S. Lee, D.H. Chung, Enhanced autophagy blocks angiogenesis via degradation of gastrin-releasing peptide in neuroblastoma cells, Autophagy 9(10) (2013) 1579-1590.
[39] D. Xiang, H. Wang, S. Sun, L. Yao, R. Li, X. Zong, G. Wang, Z. Liu, GRP receptor regulates depression behavior via interaction with 5-HT2a receptor, Frontiers in Psychiatry 10 (2020) 1020.
[40] W. van Gijn, C.A. Marijnen, I.D. Nagtegaal, E.M.-K. Kranenbarg, H. Putter, T. Wiggers, H.J. Rutten, L. Påhlman, B. Glimelius, C.J. van de Velde, Preoperative radiotherapy combined with total mesorectal excision for resectable rectal cancer: 12-year follow-up of the multicentre, randomised controlled TME trial, The lancet oncology 12(6) (2011) 575-582.
[41] M.S. Reimers, C.C. Engels, H. Putter, H. Morreau, G.J. Liefers, C.J. van de Velde, P.J. Kuppen, Prognostic value of HLA class I, HLA-E, HLA-G and Tregs in rectal cancer: a retrospective cohort study, BMC cancer 14 (2014) 1-12.
[42] Y. Zhang, M.F. Sanner, AutoDock CrankPep: combining folding and docking to predict protein–peptide complexes, Bioinformatics 35(24) (2019) 5121-5127.
[43] S. Peng, Y. Zhan, D. Zhang, L. Ren, A. Chen, Z.-F. Chen, H. Zhang, Structures of human gastrin-releasing peptide receptors bound to antagonist and agonist for cancer and itch therapy, Proceedings of the National Academy of Sciences 120(6) (2023) e2216230120.
[44] J.M. Word, S.C. Lovell, J.S. Richardson, D.C. Richardson, Asparagine and glutamine: using hydrogen atom contacts in the choice of side-chain amide orientation, J Mol Biol 285(4) (1999) 1735-47.
[45] M.-r. Zhu, D.-h. Du, J.-c. Hu, L.-c. Li, J.-q. Liu, H. Ding, X.-q. Kong, H.-l. Jiang, K.-x. Chen, C. Luo, Development of a high-throughput fluorescence polarization assay for the discovery of EZH2-EED interaction inhibitors, Acta Pharmacologica Sinica 39(2) (2018) 302-310.
[46] C.G. Da Silva, M.G. Camps, T.M. Li, L. Zerrillo, C.W. Löwik, F. Ossendorp, L.J. Cruz, Effective chemoimmunotherapy by co-delivery of doxorubicin and immune adjuvants in biodegradable nanoparticles, Theranostics 9(22) (2019) 6485.
[47] C. Da Silva, M. Camps, T. Li, A. Chan, F. Ossendorp, L. Cruz, Co-delivery of immunomodulators in biodegradable nanoparticles improves therapeutic efficacy of cancer vaccines, Biomaterials 220 (2019) 119417.
[48] S. Clement, A.G. Anwer, L. Pires, J. Campbell, B.C. Wilson, E.M. Goldys, Radiodynamic therapy using TAT peptide-targeted verteporfin-encapsulated PLGA nanoparticles, International Journal of Molecular Sciences 22(12) (2021) 6425.
[49] Y. He, R.F. de Araújo Júnior, R.S. Cavalcante, Z. Yu, T. Schomann, Z. Gu, C. Eich, L.J. Cruz, Effective breast cancer therapy based on palmitic acid-loaded PLGA nanoparticles, Biomaterials Advances 145 (2023) 213270.
[50] L. Zerrillo, K.B.S.S. Gupta, F.A. Lefeber, C.G. Da Silva, F. Galli, A. Chan, A. Veltien, W. Dou, R. Censi, P. Di Martino, Novel fluorinated poly (lactic-co-glycolic acid)(PLGA) and polyethylene glycol (PEG) nanoparticles for monitoring and imaging in osteoarthritis, Pharmaceutics 13(2) (2021) 235.
[51] L.J. Cruz, P.J. Tacken, R. Fokkink, C.G. Figdor, The influence of PEG chain length and targeting moiety on antibody-mediated delivery of nanoparticle vaccines to human dendritic cells, Biomaterials 32(28) (2011) 6791-6803.
[52] Y. Xu, W. Li, S. Chen, B. Huang, W. Pei, C. Niu, Near-infrared responsive phase-shifted nanoparticles for magnetically targeted MR/US imaging and photothermal therapy of cancer, Frontiers in bioengineering and biotechnology 8 (2020) 599107.

[53] L. Zerrillo, M.R. Gigliobianco, D. D'Atri, J.P. Garcia, F. Baldazzi, Y. Ridwan, G. Fuentes, A. Chan, L.B. Creemers, R. Censi, PLGA nanoparticles grafted with hyaluronic acid to improve site-specificity and drug dose delivery in osteoarthritis nanotherapy, Nanomaterials 12(13) (2022) 2248.
[54] T.B. KC, K. Suga, T. Isoshima, T. Aigaki, Y. Ito, K. Shiba, T. Uzawa, Wash-free and selective imaging of epithelial cell adhesion molecule (EpCAM) expressing cells with fluorogenic peptide ligands, Biochemical and biophysical research communications 500(2) (2018) 283-287.
[55] S. Rezaei, R.F. de Araújo Júnior, I.L.G. da Silva, T. Schomann, C. Eich, L.J. Cruz, Erythrocyte– cancer hybrid membrane-coated reduction-sensitive nanoparticles for enhancing chemotherapy efficacy in breast cancer, Biomaterials Advances 151 (2023) 213456.
[56] W. Beisker, E.M. Weller‐Mewe, M. Nüsse, Fluorescence enhancement of DNA‐bound TO‐PRO‐3 by incorporation of bromodeoxyuridine to monitor cell cycle kinetics, Cytometry: The Journal of the International Society for Analytical Cytology 37(3) (1999) 221-229.
[57] Z. Sheng, D. Hu, M. Xue, M. He, P. Gong, L. Cai, Indocyanine green nanoparticles for theranostic applications, Nano-Micro Letters 5 (2013) 145-150.
[58] P. Liu, Y. Tu, J. Tao, Z. Liu, F. Wang, Y. Ma, Z. Li, Z. Han, Y. Gu, GRPR-targeted SPECT imaging using a novel bombesin-based peptide for colorectal cancer detection, Biomaterials Science 8(23) (2020) 6764-6772.
[59] J.-C. Saurin, J.-P. Rouault, J. Abello, F. Berger, L. Remy, J. Chayvialle, High gastrin releasing peptide receptor mRNA level is related to tumour dedifferentiation and lymphatic vessel invasion in human colon cancer, European Journal of Cancer 35(1) (1999) 125-132.
[60] E. Sjöstedt, W. Zhong, L. Fagerberg, M. Karlsson, N. Mitsios, C. Adori, P. Oksvold, F. Edfors, A. Limiszewska, F. Hikmet, An atlas of the protein-coding genes in the human, pig, and mouse brain, Science 367(6482) (2020) eaay5947.
[61] H. Zhang, L. Qi, Y. Cai, X. Gao, Gastrin-releasing peptide receptor (GRPR) as a novel biomarker and therapeutic target in prostate cancer, Annals of Medicine 56(1) (2024) 2320301.
[62] W. Wang, K.J. Wu, K. Vellaisamy, C.H. Leung, D.L. Ma, Peptide‐Conjugated Long‐Lived Theranostic Imaging for Targeting GRPr in Cancer and Immune Cells, Angewandte Chemie 132(41) (2020) 18053-18058.
[63] K. Durkan, F.Y. Lambrecht, P. Unak, Radiolabeling of bombesin-like peptide with 99mTc: 99mTc-litorin and biodistribution in rats, Bioconjugate chemistry 18(5) (2007) 1516-1520.
[64] O. Patel, A. Shulkes, G.S. Baldwin, Gastrin-releasing peptide and cancer, Biochimica et Biophysica Acta (BBA)-Reviews on Cancer 1766(1) (2006) 23-41.
[65] P. Hildebrand, B. Werth, C. Beglinger, F. Delco, J.B. Jansen, C.B. Lamers, K. Gyr, Human gastrin-releasing peptide: biological potency in humans, Regulatory peptides 36(3) (1991) 423-433.
[66] M. Mentinova, S.A. McLuckey, Covalent modification of gaseous peptide ions with N-hydroxysuccinimide ester reagent ions, Journal of the American Chemical Society 132(51) (2010) 18248-18257.
[67] G.T. Hermanson, Bioconjugate techniques, Academic press2013.
[68] E.D. Pereira, R. Cerruti, E. Fernandes, L. Peña, V. Saez, J.C. Pinto, J.A. Ramón, G.E. Oliveira, F.G.d. Souza, Influence of PLGA and PLGA-PEG on the dissolution profile of oxaliplatin, Polímeros 26(2) (2016) 137-143.
[69] C. Zhuang, F. Tao, Y. Cui, Properties of gelatin films cross–linked by N-hydroxysuccinimide–activated furandicarboxylic acid (NHS-FDCA), Polymer Bulletin 73 (2016) 1565-1580.
[70] D. Nguyen, C. Chen, B.M. Pettitt, J. Iwahara, NMR methods for characterizing the basic side chains of proteins: electrostatic interactions, hydrogen bonds, and conformational dynamics, Methods in enzymology 615 (2019) 285-332.
[71] V. Saxena, M. Sadoqi, J. Shao, Enhanced photo-stability, thermal-stability and aqueous-stability of indocyanine green in polymeric nanoparticulate systems, Journal of Photochemistry and Photobiology B: Biology 74(1) (2004) 29-38.

[72] S. Preston, L. Woodhouse, S. Jones-Blackett, G. Miller, J. Primrose, High-affinity binding sites for gastrin-releasing peptide on human colorectal cancer tissue but not uninvolved mucosa, British journal of cancer 71(5) (1995) 1087-1089.
[73] K.A. Matkowskyj, D. Schonfeld, R.V. Benya, Quantitative immunohistochemistry by measuring cumulative signal strength using commercially available software photoshop and matlab, Journal of Histochemistry & Cytochemistry 48(2) (2000) 303-311.
[74] T. Ruginis, L. Taglia, D. Matusiak, B.-S. Lee, R.V. Benya, Consequence of gastrin-releasing peptide receptor activation in a human colon cancer cell line: a proteomic approach, Journal of proteome research 5(6) (2006) 1460-1468.
[75] R. Tell, C.A. Rivera, J. Eskra, L.N. Taglia, A. Blunier, Q.T. Wang, R.V. Benya, Gastrin-releasing peptide signaling alters colon cancer invasiveness via heterochromatin protein 1Hsβ, The American journal of pathology 178(2) (2011) 672-678.
[76] K. Tokita, S.J. Hocart, D.H. Coy, R.T. Jensen, Molecular basis of the selectivity of gastrin-releasing peptide receptor for gastrin-releasing peptide, Molecular pharmacology 61(6) (2002) 1435-1443.
[77] T.M. Lwin, M.A. Turner, S. Amirfakhri, H. Nishino, R.M. Hoffman, M. Bouvet, Fluorescence molecular targeting of colon cancer to visualize the invisible, Cells 11(2) (2022) 249.
[78] J.-M. Jung, I.J. Park, E.J. Park, G.M. Son, Fluorescence-guided colorectal surgery: applications, clinical results, and protocols, Annals of Surgical Treatment and Research 105(5) (2023) 252.
[79] Z.Y. Lim, S. Mohan, S. Balasubramaniam, S. Ahmed, C.C.H. Siew, V.G. Shelat, Indocyanine green dye and its application in gastrointestinal surgery: The future is bright green, World Journal of Gastrointestinal Surgery 15(9) (2023) 1841.
[80] R.H. Patel, A.S. Wadajkar, N.L. Patel, V.C. Kavuri, K.T. Nguyen, H. Liu, Multifunctionality of indocyanine green-loaded biodegradable nanoparticles for enhanced optical imaging and hyperthermia intervention of cancer, Journal of biomedical optics 17(4) (2012) 046003-046003.
[81] S. Zhao, L. Lee, Y. Zhao, N.-C. Liang, Y.-S. Chen, Photoacoustic signal enhancement in dual-contrast gastrin-releasing peptide receptor-targeted nanobubbles, Frontiers in Bioengineering and Biotechnology 11 (2023) 1102651.
[82] P. Zhao, M. Zheng, C. Yue, Z. Luo, P. Gong, G. Gao, Z. Sheng, C. Zheng, L. Cai, Improving drug accumulation and photothermal efficacy in tumor depending on size of ICG loaded lipid-polymer nanoparticles, Biomaterials 35(23) (2014) 6037-6046.
[83] M. Tayama, T. Inose, N. Yamauchi, K. Nakashima, M. Tokunaga, C. Kato, K. Gonda, Y. Kobayashi, Fabrication and fluorescence imaging properties of indocyanine green-loaded poly (lactic-co-glycolic acid) nanoparticles, Colloid and Polymer Science 299(8) (2021) 1271-1283.
[84] C. Zheng, M. Zheng, P. Gong, D. Jia, P. Zhang, B. Shi, Z. Sheng, Y. Ma, L. Cai, Indocyanine green-loaded biodegradable tumor targeting nanoprobes for in vitro and in vivo imaging, Biomaterials 33(22) (2012) 5603-5609.
[85] Q. Chen, L. Xu, C. Liang, C. Wang, R. Peng, Z. Liu, Photothermal therapy with immune-adjuvant nanoparticles together with checkpoint blockade for effective cancer immunotherapy, Nature communications 7(1) (2016) 13193.
[86] V. Saxena, M. Sadoqi, J. Shao, Enhanced photo-stability, thermal-stability and aqueous-stability of indocyanine green in polymeric nanoparticulate systems, Journal of Photochemistry & Photobiology, B: Biology 1(74) (2004) 29-38.
[87] K. Kim, M.-H. Park, Role of Functionalized Peptides in Nanomedicine for Effective Cancer Therapy, Biomedicines 12(1) (2024) 202.
[88] J. Dai, M. Ashrafizadeh, A.R. Aref, G. Sethi, Y.N. Ertas, Peptide-functionalized,-assembled and-loaded nanoparticles in cancer therapy, Drug Discovery Today 29(7) (2024) 103981.